

Research on the Application of Vortex Beam in Ptychography

CHEN JIE

MSc (by research)

University of York

Physics

October 2020

Abstract

Ptychography is a coherent diffraction technology, which is not limited by sample size and has the advantages of high imaging quality, strong portability, and low stability requirements for optical platform. It has been experimentally confirmed in the visible light domain, X-ray and other different frequency bands. The ptychography system has a wide application prospect in the fields of microimaging, three-dimensional morphology measurement and information security. However, many researches on ptychography are still in the preliminary theoretical stage and there is none research on its combination with vortex beam, and the key parameters affecting the imaging performance are still not to be studied. This thesis first briefly introduces the research background, significance, the basic concepts, development and application of ptychography and vortex beam. Then, it introduces the theoretical basis supporting its use, including computer-generated hologram (CGH), beam steering and the computing algorithm of ptychography. On this basis, this thesis presents the following innovative research:

An optical ptychography set-up, with a spatial light modulator as the core device, is designed to facilitate the flexible production of different types of optical probe, such as the generation of conventional beams and vortex beams; flexible adjustment of the order and defocus of vortex beams, etc., so as to realize their experimental exploration. Experiments show that vortex beams have a higher imaging quality in ptychography, and the topological charge number and defocus of vortices also affect the reconstruction quality of the samples to a certain extent. Therefore, these parameters can be adjusted according to the experimental requirements to achieve the best recovery quality of information about the samples in the actual experimental operation.

Contents

1	Introduction	1
1.1	Vortex beam	1
1.2	Ptychography	3
1.3	Project research background and significance	5
1.4	Structure of this dissertation	7
2	Basic concepts and theory	8
2.1	Historical overview of vortex beam research	8
2.2	Historical overview of ptychography research	9
2.2.1	Three-dimensional ptychography microscopy	9
2.2.2	Ptychography for optical image encryption	11
2.2.3	Fourier ptychography microscopy	12
3	Experimental Principles	14
3.1	The working principle of SLM	14
3.2	Holography	15
3.3	Vortex beam production method	16
3.4	Beam deflection by blazed grating	19
3.5	Reconstruction algorithm for ptychography	20
3.5.1	PIE algorithm	20
3.5.2	ePIE algorithm	23
4	Calibration of SLM	24
4.1	Construction of experimental platform	24
4.2	Determination of phase modulation range	25
4.2.1	Phase grating diffraction characteristics	26
4.2.2	Experimental set up	29
4.2.3	Experimental result	29
4.2.4	Results and Analysis	33
4.3	SLM phase modulation calibration	35
4.3.1	Experimental result	37
4.4	Combination of the two methods	38

5	Application of SLM in vortex beam ptychography	42
5.1	Experimental set-up and data collection	42
5.1.1	Design principle of imaging system	42
5.1.2	Design scheme of imaging system	44
5.1.3	Data collection	49
5.2	Reconstruction and quantification of quality	52
5.3	Effect of defocus, effect of topological charge of the vortex beams	59
6	Conclusion and future work	61
6.1	The main work and research results	61
6.2	Future research directions	61
A	Mathematical derivation of diffraction pattern of a binary phase grating	63
B	Mathematical derivation of diffraction pattern of a Bowman phase grating	65
C	Matlab code to generate CGH and receive diffraction pattern	67
D	Matlab code for ePIE algorithm function	70

List of Figures

1.1	helical beam with different topological charge. columns show the helical structures, phase-front and intensity of the beams. black maps to a phase value of 0, while white maps to a phase value of 2π , Figure courtesy of [1]	2
1.2	Diagram of Ptychography (a) Optical Set-up (b) Probe overlapping position (c) Amplitude recovered from Ptychography. Figure courtesy of [2]	4
2.1	Slices selected from the reconstructed phase distribution of a complex amplitude type mass algae specimen with a total thickness of $150\mu m$. The slice (a)-(h) corresponds to the 1, 3, 5, 11, 17, 21, 24 and 28 faces of the 34 slices. The distance between adjacent faces is $4.7\mu m$. The color-bar in (a) indicates the phase shift (radians). Figure courtesy of [3]	10
2.2	(a)-(d) are the slices selected from the phase distribution reconstructed from the complex amplitude embryo tip specimens, (e)-(h) are the data collected from the same embryo tip specimens under a fluorescent confocal microscope. The color-bar in (a) indicates the phase shift (radians). The color-bar in (e) indicates the florescence intensity (a.u.). Figure courtesy of [3]	10
2.3	Schematic diagram of stacked imaging encryption system. Figure courtesy of [4]	11
2.4	The amplitudes and phase distributions decrypted by three different types of probes. (a) and (b) correspond to pure amplitudes; (c) and (d) correspond to pure phases; and (e) and (f) correspond to complex amplitudes. Figure courtesy of [4]	12
2.5	Fourier ptychography device prototype. (a) Device diagram, (b) LED array and microscope used in the experiment, (c) USAF resolution test diagram, magnification of the original image, and reconstruction of the same area using the Fourier domain lamination imaging microscopy device. Figure courtesy of [5]	13
3.1	Forked gratings with different order topological charges, black maps to 0 grayscale and white maps to 255 grayscale	18

3.2	Introducing linear phases change on the incoming plane wave causes a tilt on its direction. Consequently, it produces a 1D transverse shift of the spot at the focal plane of the lens. when phases change linearly along the y-axis, the optical wavefront is tilted by an angle, θ , due to a linear phase shift, L is the period of the phase, producing a difference of λ on the optical path. P is the pixel width. The phase modulation of SLM can be equivalent to that of prism.	19
3.3	(a) and (b) represent the blazed grating(left) with different pixel periods and its corresponding diffraction pattern(right), respectively, and the red line clearly indicates the steering of light in the horizontal direction. order topological charges, black maps to 0 grayscale and white maps to 255 grayscale	20
3.4	Block diagram of PIE algorithm	21
4.1	The optical system used in the experiment is mainly used to measure the far-field diffraction pattern produced by the hologram displayed on the SLM by a computer. The beam from the laser is expanded by the lenses 1 and lens 2, being processed into polarized light by a polarizer and modulated by SLM, and then Fourier transformed by a lens 3. Finally, using the camera in the Fourier plane of the SLM to measure the diffraction pattern . . .	25
4.2	One element of the binary grating	26
4.3	Diffraction pattern due to the binary grating of Fig .4.2	27
4.4	Relationship between gray level and normalised intensity of zero-order diffraction spot	28
4.5	The 0-order diffraction beam spot of binary grating (left) and the reference 0-order beam spot without grating structure(right). . .	29
4.6	Longitudinal strip binary grating and evolution of the experimental intensities of the zero-order beam spots when increasing the gray value of the 'white' strips.(for an incident beam with vertical polarization)	30
4.7	The normalized 0th order diffraction beam (vertical polarization) as a function of the maximum gray level of the binary grating, together with a curve fitting of the data using $a + cxcos(graylevel)$	31
4.8	Longitudinal strip binary grating and evolution of the experimental intensities of the zero-order beam spots when increasing the gray value.(for an incident beam with horizontal polarization). . .	32
4.9	The normalized 0th order diffraction beam(horizontal) as a function of the maximum gray level of a binary grating, together with a curve fitting of the data using $a + c \times cos(graylevel)$	33
4.10	The phase response curve (phase change vs.maximum gray level).	34

4.11	(a) A set of ramps wrapped at 2π . The x variable represents one spatial coordinate on the SLM. (b) A real SLM can reach a maximum value of the phase ϕ_{max} which is different from 2π . (c) By changing the contrast, it is possible to obtain a phase-ramp which is as similar as possible to the ideal one. Figure courtesy of [6]	35
4.12	The x variable represents one spatial coordinate on the SLM. (a) The phase modulation that an ideal blazed grating can achieve. (b) A experimental SLM does not produce the desired unwrapped phase. (c) By changing the contrast, it is possible to obtain an unwrapped phase which is as similar as possible to the ideal one.	35
4.13	By adjusting the contrast, it will affect the hologram sent to the SLM. (a) Ideal situation with $C = 1$. (b) By increasing the contrast we increase the number of pixels that will be black or white on SLM (c) When $C = 255$ every pixel must be black or white, no matter what hologram we send into the SLM, so we have a binary hologram	36
4.14	One element of Bowman blazed grating under different contrast	36
4.15	Bowman blazed grating under different contrast	37
4.16	The diffraction patterns (vertically aligned) due to Bowman Blazed Grating as a function of the contrast values. The patterns were recorded at a defocus to accommodate the the finite dynamical range of the recording CCD camera.	37
4.17	Evolution of the experimental intensities of the zero and ± 1 orders spots when increasing the contrast (normalized against the 0^{th} order beam without diffraction grating contrast, plotted as a function of the contrast parameter.)	38
4.18	The phase modulation curve of the spatial light modulator (red curve drawn through experimental data). Also plotted is the idealised spatial light modulation curve (blue).	39
4.19	(1)Ideal situation with $C = 1$ (2)As discussed in Fig.4.13, the relationship between input gray and output gray is changed by increasing the contrast, thus increasing the number of pixels that will appear black or white on the SLM	40
4.20	By adjusting the contrast, the original phase modulation curve was closer to the ideal 6PI phase modulation curve	41
5.1	A diagram of a probe scanning a sample during ptychography. Figure courtesy of [7]	43
5.2	Overlapping scanning of a light probe on the sample surface. G is scanning step and E is probe width.	43
5.3	The optical set-up for imaging the scanning probe. The slit is used to block the unwanted diffracting beams.	44
5.4	Optical set-up for the ptychography experiment. $L4$ and $L5$ are adjusted to either image the probe or the diffraction pattern of the probe.	45

5.5	The optical set-up for ptychography with the sample placed in a defocused position with respect to the focal plane of the probe. Where d_1 is the focal length of L3, d_2 is the distance from the focus of L3 to the sample, d_3 is the distance from the probe focus to L4, d_4 is the distance from L5 to CCD camera, and d_5 is the distance from CCD camera plane to focal point pf L5.	46
5.6	(a) is the grating to achieve vertical deflection required by the experiment. By combining the fork gratings and the blazed gratings, and by changing the pixel period of the gratings, a grating which can realize both vertical scanning and vortex light generation is obtained. (b) is the position of the probe corresponding to the two gratings. The red line clearly reflects the change of the position of the probe in the vertical direction(Vertical scanning).	47
5.7	(a) is the grating to achieve horizontal deflection required by the experiment. By combining the fork gratings and the blazed gratings, and by changing the pixel period of the gratings, a grating which can realize both horizontal scanning and vortex light generation is obtained. (b) is the position of the probe corresponding to the two gratings. The red line clearly reflects the change of the position of the probe in the horizontal direction(Horizontal scanning).	48
5.8	Probe scanning range calculated from data	49
5.9	The image of the scratched area taking using mobile phone (Huawei, P30, camera apps). The scale bar is calculated using the information about the physical size of the sample and the pixel size of the sample in the image.)	50
5.10	The montage of the diffraction pattern of a normal (non-vortex) beam (by setting $l=0$) as it scans the sample in 7×7 positions. . .	50
5.11	Diffraction of the sample by vortex beam of order 4.	51
5.12	the diffraction patterns of different order vortex beam at the same position	51
5.13	Diffraction pattern of vortex beam with different focus at the same position for $\ell = 5$	52
5.14	The phase reconstruction images of the samples were compared by using the vortex probe(a) and the non-vortex probe(b), the yellow line represents the sampling area of the line profile, (c) is the real image of the scratch structure in the same scale	52
5.15	The sample is reconstructed by using vortex beam and non-vortex beam, extracting a line profile across a specific scratch feature to obtain the gray distribution of the specific line. The horizontal axis represents the length of the line, and the vertical axis reflects the gray values at different positions.	53
5.16	The amplitudes(left) and phases(right) of the sample when reconstruction is carried out.	54
5.17	The amplitudes(left) and phases(right) of the estimate of the probe after the reconstruction.	55

5.18	The comparison of the phase reconstructed images of the sample, for different defocus condition, the yellow line represents the sampling area of the line profile.	56
5.19	Line profiles are drawn across specific scratch characteristics under different defocus conditions. The horizontal axis represents the length of the line, and the vertical axis reflects the gray values at different positions.	56
5.20	Sample Phase reconstruction of different ℓ vortex beam (Defouse=1.0mm), the yellow line represents the sampling area of the line profile.	57
5.21	The amplitudes(top) and phases(bottom) of the probe when reconstruction is completed, for different ℓ	58
5.22	Line profiles are drawn across specific scratch characteristics under different order conditions. The horizontal axis represents the length of the line, and the vertical axis reflects the gray values at different positions.	58

Declaration

I hereby declare that this dissertation is the result of my own work, except where explicit reference is made to the work of others, and has not been presented in any previous application for a degree at this or any other institution
Signed:..... CHEN JIE

Acknowledgements

I would like to thank my supervisor, Professor Jun Yuan, for his support and encouragement. During my study, his encouragement made me grow up little by little. His suggestions on experimental operations and code writing were very helpful, and he also discussed experimental mathematics with me, which was very helpful to my experimental results. In addition, I would also like to thank Yuan-Hung Lo of University of California for providing the ePIE algorithm code, under which I was able to get the experimental results smoothly after modification. Finally, I would like to thank my parents for their support (financially and otherwise!). Otherwise I won't have the chance to study in University of York.

Chapter 1

Introduction

1.1 Vortex beam

Vortex structures are a natural phenomenon. Examples include hurricanes in the atmosphere [8], “vortices” in classical fluid mechanics [9], and super-fluid helium in quantum systems [10]. For the wave phenomenon, the wave with phase singularity and rotating around the singularity is called vortex. The topological charge ℓ refers to the number of phase singularities or the number of branches in the vortex space (the number of tooth intervals). The optical vortex is an electromagnetic wave with a spiral wavefront, In theory, a single photon carries angular momentum $\ell\hbar$ (ℓ is the topological charge and can take any integer value, \hbar is Planck’s constant). The optical vortex is also called “twisted light”. The wavefronts of a vortex beam have a helical structure. The three-dimensional phase structure is shown in Fig. 1.1.

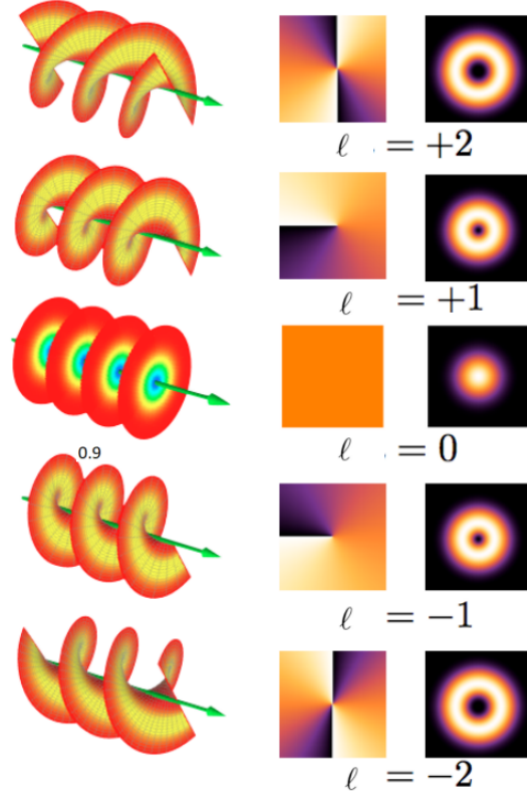


Figure 1.1: helical beam with different topological charge. columns show the helical structures, phase-front and intensity of the beams. black maps to a phase value of 0, while white maps to a phase value of 2π , Figure courtesy of [1]

Vortex beams are typified by two types: the Laguerre-Gaussian mode and the Bessel-Gaussian mode [11–15]. The field of Laguerre-Gaussian beam in a plane perpendicular to the propagation direction can be expressed as [16]:

$$E(r, \theta) = \left(\frac{\sqrt{2}r}{\sigma} \right)^l \exp\left(-\frac{r^2}{\sigma^2}\right) \exp(-il\varphi) \quad (1.1)$$

The field of a Bessel in a plane perpendicular to the propagation direction beam can be expressed as [17]:

$$E(r, \theta) = J(\alpha r) \exp(il\varphi) \quad (1.2)$$

Where σ is the spot size, l is the topological charge, r is the modulus of the plane position vector of the light source, and φ is the azimuth angle of the light source plane position vector, J is a Bessel function of the first kind. It can be seen from the above expression that both Laguerre-Gaussian beams

and higher-order Bessel beams have an azimuthal phase term $\exp(i\ell\varphi)$. Such a beam carries the orbital angular momentum $\ell\hbar$, and there is a phase singularity on the optical axis, that is, the phase is indeterminate on the optical axis where the beam intensity is zero; On the section perpendicular to the optical axis, there is a beam intensity distribution of the bright ring containing dark spots, that is, the dark center beam (shaped like doughnut) [18, 19].

1.2 Ptychography

Ptychography is a coherent diffraction imaging (CDI) technology that records the intensity information of an object and calculates the phase relationship between the interference parts of different scattered waves. As it is a lens-free imaging technique, it can improve the resolution and achieve performance that traditional imaging technology cannot reach. Unlike traditional imaging techniques, ptychography does not need a stable reference light wave and the interferometer that is needed is only the object itself that causes the diffraction pattern. The concept of ptychography was coined by Hegerl and Hoppe in 1970 [20]. However, it was difficult to expect proof-of-principle experiments in the atomic-scale short wavelength range unless it could be achieved by observing crystal objects under a scanning transmission microscope. Hoppe and Strube gave an ideal proof experiment in the visible light domain at that time, but since there was no scanning transmission microscope at that time, they could only make an idea at that time [21]. At the time, Ptychography did not seem to offer any intuitive improvement over existing imaging, diffraction, and holography techniques. In 1992, Rodenburg and Bates gave various strategies to perform antiphase recovery calculations, including direct Wigner distribution deconvolution (WDD), and predicted the advantages of Ptychography in phase recovery [22]. In 1995, Nellist et al. successfully conducted a proof-of-principle experiment of ptychography and verified that ptychography does have a unique and important advantage over other phase recovery and imaging technologies: it is not limited by coherent diffraction [23]. The constraint of wide information limitation, known as the “information limitation”, is still the final obstacle to obtaining optimal electronic imaging [23]. In 2004, Faulkner and Rodenburg improved the ptychography technique and named it Ptychographic Iterative Engine (PIE) [24]. After continuous improvement by scholars, ptychography has since been experimentally verified in different wavelengths such as the visible light domain and X-ray [25–29], and improved algorithms have been developed to improve imaging quality and computing speed [30, 31]. Due to its excellent performance, ptychography has been applied to many fields.

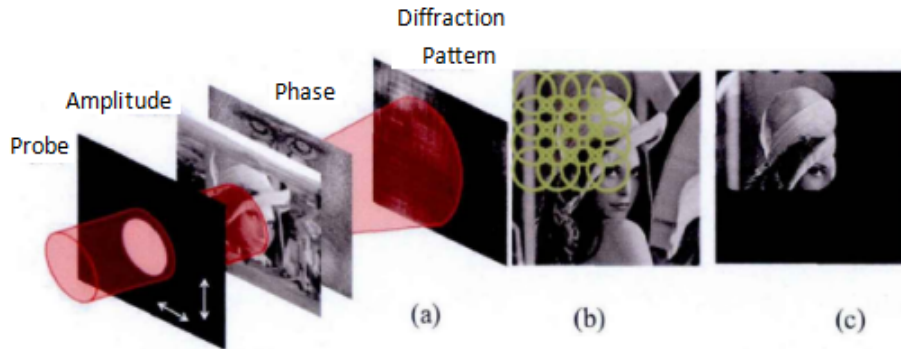


Figure 1.2: Diagram of Ptychography (a) Optical Set-up (b) Probe overlapping position (c) Amplitude recovered from Ptychography. Figure courtesy of [2]

Ptychography is a coherent diffraction technique. In its modern form, the imaging data is obtained from a series of diffraction patterns generated by the interaction between the collected object function and the wavefront of the local probe [32]. The probe can be obtained by focusing the light beam by a lens, or an illumination probe [33] can be generated by a beam shaping element. Every time you move the sample or probe, you must ensure that the illuminated area overlaps. Fig.1.2(a) shows a schematic diagram of ptychography. Through a series of diffraction patterns collected from different spatial configurations of the object and the probe, the corresponding phase recovery algorithm can be used to reconstruct the complex amplitude information of the object. The key to this stack scanning is that every time a “layer” of the sample is illuminated (the part of the sample that is illuminated each time), it must partially overlap with other adjacent “layer”, A schematic diagram of the overlapping position of the illumination beams in stack scanning is shown in Fig.1.2, with layers in 4 rows and 4 columns. A digital image sensor (such as a CCD) is used to collect the corresponding diffraction intensity pattern of each “layer” after passing through the entire system, and then a phase recovery algorithm can be designed to reproduce Construct the complex amplitude information of the sample. Different from most phase recovery algorithms, each layer’s complex amplitude is constrained by the distribution of other layers during the reconstruction, so that the recovered complex amplitude information is the common solution of all layers. In this way, the algorithm can quickly converge and the ambiguity of solutions can be eliminated. Fig.1.2(c) is the amplitude distribution of the sample recovered by the stacked imaging, and the reconstruction range can be seen in Fig.1.2(b).

Compared with other technologies, ptychography has a faster convergence speed and higher imaging quality, so it can be applied to situations requiring high resolution and high imaging quality. However, as stated, the key to ptychography is to collect a series of diffraction patterns for image reconstruction by moving the probe. The probe needs to be precisely controlled during the moving and

scanning process, and the data acquisition process is time-consuming. [25, 34].

1.3 Project research background and significance

Since ancient times, people have been trying various methods to break through the limits of the human eye, hoping to uncover the mystery of the vast universe, and also eager to observe ultra-fine objects. Since the invention of the astronomical telescope and optical microscope in the 17th century, optical imaging technology has greatly promoted the progress of human civilization in exploring and discovering the mysteries of the unknown world. All along, people have been developing various new technologies to improve the imaging quality of optical systems. However, one factor restricting the development of ultra-high imaging quality is the improvement of resolution. At the end of the 19th century and the beginning of the 20th century, scientists Abbe and Rayleigh proved from the wave theory of light that in optical imaging systems, the diffraction effect of light will cause the image of an ideal point-like object to no longer be an ideal geometric image point; instead, it will be a spot of a certain size, that is, the Airy disk. If the distance between two point-like objects is too small, their Airy disks will overlap and the two objects will not be distinguishable in the image. That is to say, there is a resolution limit in the classical optical system, which is a diffraction limited system.

According to the Rayleigh criterion, when the center of one Airy disk coincides with the first dark ring of another Airy disk, the two points can be distinguished exactly [35]. In a photographic system, the minimum distance at which two points are resolvable is related to the wavelength of the incident light wave, the focal length of the lens and the size of the aperture; in the microscopic system, to improve resolution, the wavelength can be reduced or the aperture (or numerical aperture) can be increased [36]. In addition, the aberrations of lenses also affect the resolution. Although small aberration lenses are easy to manufacture in the visible light range, they are difficult to manufacture for short wavelengths [37]. Therefore, many scholars began to explore lensless imaging technology to solve the problem that high-quality lenses are difficult to manufacture.

Improving the resolution is only a difficult problem in optical imaging technology. At the same time, because the existing optical recording materials and digital image sensors only respond to light intensity, a key problem to be solved in many development fields of modern optics is how to recover the phase information from the intensity pattern (amplitude) of a recorded sample, which is known as the complex phase recovery problem. [38]. As early as 1952, Sayre made a theoretical study on whether phase distribution information can be detected from intensity distribution according to the Nyquist-Shannon sampling theorem [39]. The results show that the phase information can be recovered from the diffraction intensity distribution under certain conditions.

Among any phase retrieval techniques, holography is one of the most widely studied techniques in terms of depth and breadth. Holography was proposed by

Gabor in 1948 in his paper “A new microscopic principle”. Holographic technology uses the interference and diffraction characteristics of light waves, through the introduction of a beam of reference light and object light wave for interference, recording the intensity information of the interference field, and then using the reference light to reproduce the intensity distribution, the amplitude and phase of all information representing the object can be recovered. In short, the technique involves interference recording and diffraction reconstruction. It is the same as the recorded intensity signal, but the total technique can reproduce the complex amplitude information of the object. Later, the emergence of the laser brought a good coherent light source, which created excellent conditions for the practical operation and application of holography. Therefore, there was an upsurge of holographic research in the scientific community. With the development of computer technology and digital image sensor technology, digital holography technology based on digital image sensors and computer image processing technology has aroused the interest of experts and scholars all over the world, and many new applications have appeared. There are digital holographic microscopy techniques that can perform digital microscopic imaging of phase or three-dimensional objects [40, 41], and digital holographic interferometric wavefront measurement techniques [42, 43]. Digital holography can also be used in image encryption and hiding [44], image recognition [45], biomedical [46] and other fields.

However, there are very strict conditions in the implementation of holography. In the process of hologram formation, the holographic platform needs maintain very high stability; vibration at the level of even one tenth of the wavelength will seriously affect the quality of the interferogram. In recent years, in order to improve the accuracy of phase recovery, many improved phase recovery algorithms have been developed, such as the multi diffraction circle sample phase recovery algorithm [47], oversampling algorithm [48], and so on. Among them, the ptychography technique proposed by Hoppe in 1969 is worthy of our attention [49, 50]. Hoppe’s method solves the problem that the phase recovered from a single diffraction pattern is relatively blurred. The beam used to irradiate a sample and produce a diffraction pattern is moved to different positions of the sample by moving the small hole from which it exits or the position of the beam is unchanged and the object is moved. The diffraction patterns corresponding to different positions are recorded, then stacked together to produce a comprehensive image. Ptychography technology also solves the problem of stable reference light in holography. However, Hoppe’s work was not taken seriously for a long time. The reasons are as follows: (1) at that time, the development of phase retrieval was still in its infancy, and the efficient and practical phase recovery algorithm had not yet come out; thus, although the idea of ptychography was a good one, it was difficult to implement. (2) It was not until 2004 that Faulkner and Rodenburg began to re-study Hoppe’s work on ptychography, and combined with the phase recovery algorithm, proposed a greatly improved iterative algorithm for ptychography. It was then that the ptychography began to receive widespread attention from people [24, 51].

1.4 Structure of this dissertation

The thesis is divided into six chapters, the specific structure and chapter arrangement are as follows: Chapter 1 is an introduction. This chapter briefly introduces the research background, significance and basic concepts of vortex light and stacked imaging.

Chapter 2 describes the current development process of vortex light and stack imaging.

Chapter 3 mainly describes the key equipment used in the experiment and the principles of use, and introduces how to generate a vortex beam and realize ptychography.

Chapter 4 introduces the methods of adjusting the spatial light modulator. In this thesis, two such methods are used for calibration, and a comparison is made between them.

Chapter 5 presents the combination of the vortex beam and ptychography to image the material, where the material is ultimately imaged successfully, and the factors that affect the imaging quality are discussed.

Chapter 6 is the conclusion and prospects of this research. This chapter mainly summarizes the research work of each part of the thesis, briefly expounds some existing problems in the experiment that need to be further studied, and puts forward the future research prospects.

Chapter 2

Basic concepts and theory

2.1 Historical overview of vortex beam research

The study of optical vortices can be traced back to 1838. Airy discovered that after a beam passed through a lens, an abnormal halo could be observed on its focal plane. However, due to the lack of advanced technology at that time, the cause of this anomaly was not studied further [52]. In 1919, Ignatovskii conducted further analysis of Airy's abnormal halo, and found that the direction of energy flow around the halo was opposite to its initial direction [53]. In 1952, Braubek and Laukien interfered the plane wave with the reflected beam of the semi-reflective screen, and found the existence of vortices in the interference field [54]. In 1959, Richard et al. analyzed the distribution of energy flow in the focal plane and calculated the vector information of focus position [55]. Then, in 1967, Boivin et al. discovered the existence of a linearly rotating vortex around the energy flow. It was later proven that vortices also exist in the light wave field [56].

Starting in the 1970s, further characteristics of optical vortices began to be uncovered seriatim. In 1974, Nye et al. proposed that dislocation structure also exists in the light field by comparing with the dislocation structure of crystals [57]. There are two dislocation structures, one is continuous spiral dislocation, the other is discontinuous dislocation. It was pointed out for the first time that the root cause of optical vortices is dislocation phase. This study laid a foundation for the understanding of optical singularities in the future. Later, Soskin et al. found that if a large part of the optical vortex is obscured, the beam itself will recover to some extent during transmission [58]. In 1981, Baranova et al. found that optical vortices exist in speckle fields [59]. In 1989, Couillet et al. found that there was a singularity of zero electric field intensity in a relatively large Fresnel laser cavity with a phase change of 2π per turn instead of being constant. They introduced the term "optical vortices" for the first time to describe the situation and theorized the phenomenon. This study provided a qualitative leap in the development of optical vortices [60]. In 1992,

Swartzlander et al. first observed the existence of optical vortex solitons in nonlinear Kerr media [61]. In the same year, Allen et al. confirmed that each photon in the vortex has orbital angular momentum according to Maxwell's equation [11]. In 1995, He et al. first realized the manipulation of copper oxide particles by using optical vortices, confirmed the transfer of orbital angular momentum to particles in optical vortices, and observed the rotation of particles [62]. In 1997, Simpson et al. used optical vortices to rotate the particle itself, and defined this operation as "optical wrench" [63].

Optical vortices have great potential and application prospect, and have been studied by many scholars. The phase of optical vortices containing singularities is a new method for image edge enhancement [64]. In addition, the photons containing orbital angular momentum have received more and more attention for the application in quantum computing [65], remote sensing [66] and other fields.

2.2 Historical overview of ptychography research

As a key technology of coherent diffraction, ptychography technology is not limited by sample size and has high imaging resolution, strong portability, and low requirements on the stability of the optical platform. Therefore, it has received extensive attention in recent years, with research developing quite rapidly since its inception. At present, research on ptychography focuses on expanding the scope of application, pursuing its application in the field of extreme physics and obtaining corresponding detection result.

2.2.1 Three-dimensional ptychography microscopy

Ptychography is limited to transparent objects; the illumination beam needs to penetrate through the sample for imaging, which limits the thickness of the sample. In the visible region, the thickness of the sample can not exceed tens of microns to achieve resolution on the micron level. To address this issue, in 2014, T.M. Gordon et al. invented a 3-dimensional ptychography microscopy technology [3]. By cutting the sample into several parts along the axial direction, the thickness limit of the sample can be relaxed. The optical slicing of crude sugar can be realized by using a single stacked imaging data acquisition device. They used an improved version of the optical microscope to collect data. The thickness of the slices can be from $2\mu m$ to $150\mu m$, and the number of imaging slices has been increased from 5 to 34 now. In addition, there is a strong phase contrast, so it is not necessary to dye the samples. Fig. 2.1 and Fig. 2.2 show the experimental results of Gordon et. al, which strongly demonstrate the advantages of the technique. They use the traditional microscope and h-dimensional stacked imaging algorithm to achieve high-quality imaging of thick slices [3].

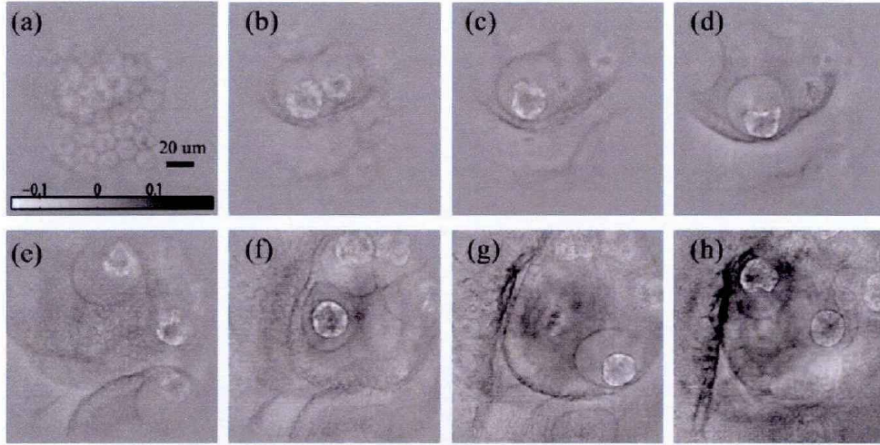


Figure 2.1: Slices selected from the reconstructed phase distribution of a complex amplitude type mass algae specimen with a total thickness of $150\mu m$. The slice (a)-(h) corresponds to the 1, 3, 5, 11, 17, 21, 24 and 28 faces of the 34 slices. The distance between adjacent faces is $4.7\mu m$. The color-bar in (a) indicates the phase shift (radians). Figure courtesy of [3]

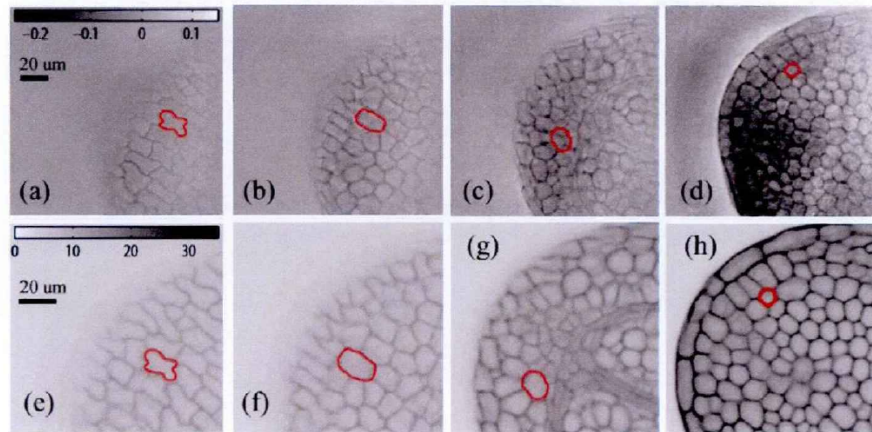


Figure 2.2: (a)-(d) are the slices selected from the phase distribution reconstructed from the complex amplitude embryo tip specimens, (e)-(h) are the data collected from the same embryo tip specimens under a fluorescent confocal microscope. The color-bar in (a) indicates the phase shift (radians). The color-bar in (e) indicates the fluorescence intensity (a.u.). Figure courtesy of [3]

2.2.2 Ptychography for optical image encryption

In 2013, Shi et al. used laminated imaging in optical image encryption, and realized the combination of ptychography and information security [4]. Ptychography can be applied to almost all encryption systems. Compared with the traditional double random phase encryption method, the introduction of the probe increases the key space, which significantly improves the security of the system. Based on the double random phase encryption system, Shi et al. provided a simulation experiment proof of ptychography for optical image encryption. Fig. 2.3 presents the schematic diagram of the proposed ptychography encryption system. Fig.2.4 shows the decryption amplitude and phase distribution of three different types of probes (pure amplitude, pure phase, and complex amplitude). In addition, no interference is needed in the whole encryption process, which reduces the complexity of the encryption system and is helpful to the realization of the optical encryption system.

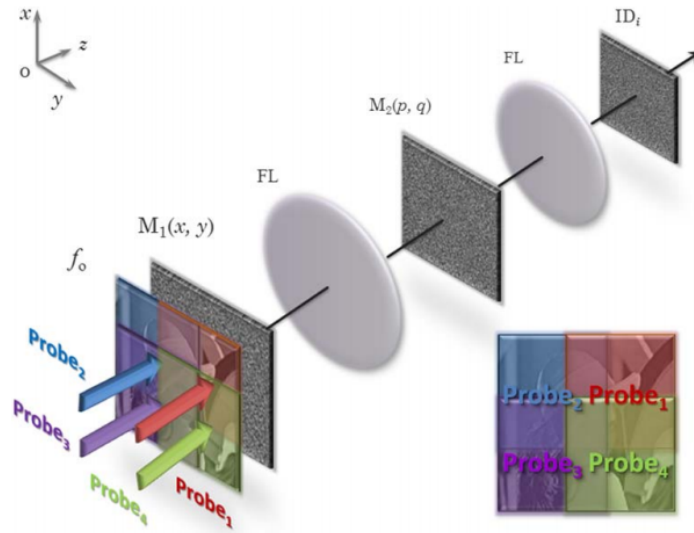


Figure 2.3: Schematic diagram of stacked imaging encryption system. Figure courtesy of [4]

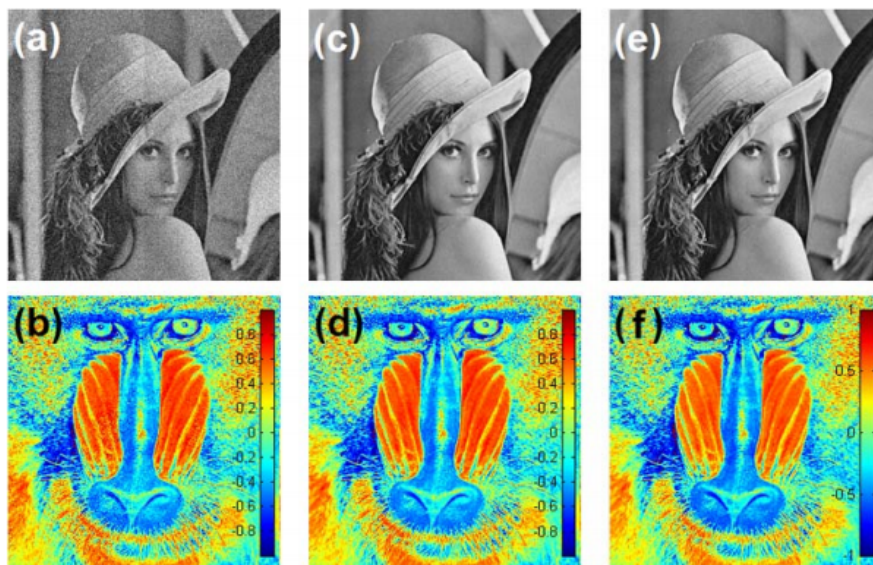


Figure 2.4: The amplitudes and phase distributions decrypted by three different types of probes. (a) and (b) correspond to pure amplitudes; (c) and (d) correspond to pure phases; and (e) and (f) correspond to complex amplitudes. Figure courtesy of [4]

2.2.3 Fourier ptychography microscopy

In 2013, Zheng founded the wide-field-of-view, high-resolution Fourier Ptychography Microscopy (FPM) technique, which enables multi-angle lighting to a series of lighting probes collected within the Fourier domain. The iterative algorithm is used to process the low-resolution intensity image and generate the complex amplitude image with wide field of view and high resolution [5]. In addition, FPM can also correct aberrations due to the introduction of wavefront correction technology, and digitally extend the depth-of-field of the microscope without being restricted by the optical system. They also produced a FPM device, as shown in Fig. 2.5(b), with a resolution of $0.78\mu m$, a field-of-view of about $120mm^2$, and a depth-of-field of $0.3mm$ (taking the wavelength of $632nm$ as an example) with a constant resolution. As can be seen from the comparison between Fig. 2.5(c) and Fig. 2.5(d), the resolution of reconstructed image by FPM device is greatly improved.

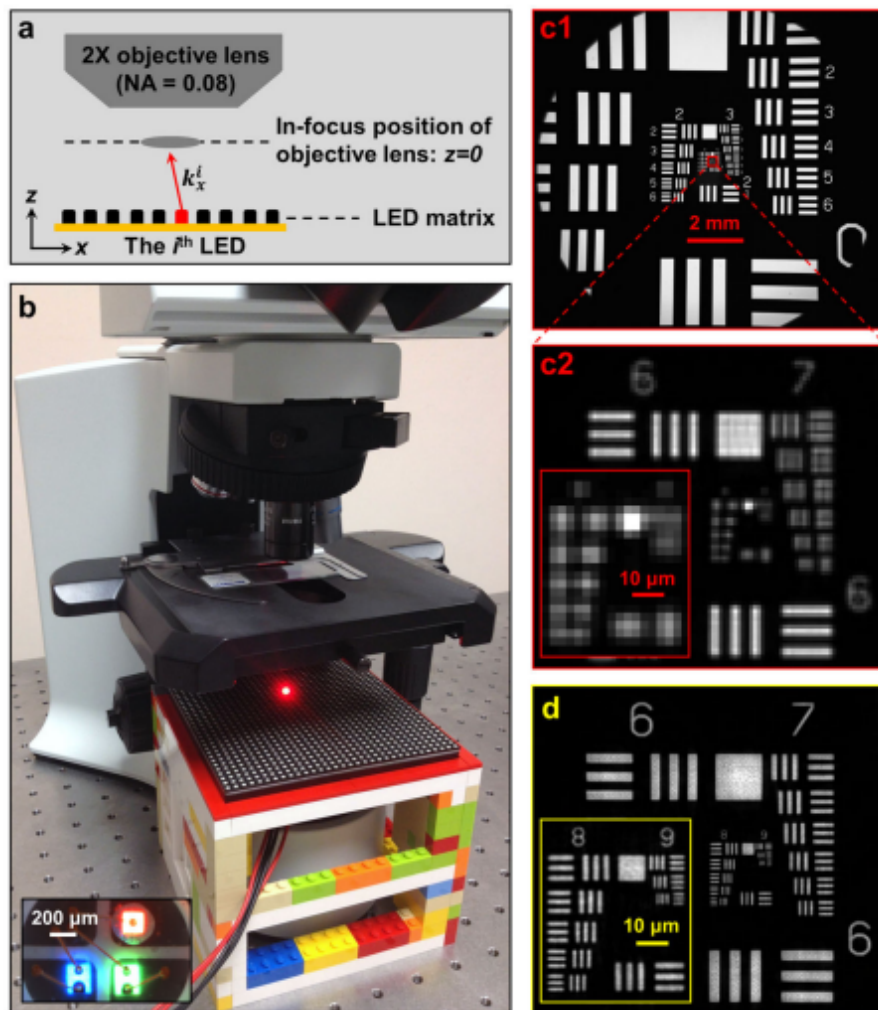


Figure 2.5: Fourier ptychography device prototype. (a) Device diagram, (b) LED array and microscope used in the experiment, (c) USAF resolution test diagram, magnification of the original image, and reconstruction of the same area using the Fourier domain lamination imaging microscopy device. Figure courtesy of [5]

Chapter 3

Experimental Principles

Ptychography is an important coherent diffraction imaging technique [67], which has the advantages of high quality phase retrieval and is not limited by sample size. It has been used in X-ray [68], optical [69] and electronic fields [29]. The fact is Ptychography experiments are mostly combined with X-rays at present, and few studies have combined with vortex beam, while vortex beam has an excellent performance in imaging, so it is particularly important to combine vortex beam with contrast-enhanced ultrasound. In order to compare the imaging properties of ptychography with conventional and vortex probes, the design of the imaging system should strongly consider both the generation of the vortex beam and the realization of ptychography. Therefore, the spatial light modulator (SLM) is used as the key equipment in this experiment. This chapter is divided into three main parts. The first part describes the working principle of SLM, the second part describes the production method of vortex beam, the third part introduces how to achieve beam deflection.

3.1 The working principle of SLM

Each pixel of a liquid crystal spatial light modulator (LC-SLM) consists of a nematic liquid crystal layer and an electrode, the nematic liquid crystal has an electronic birefringence effect. Nematic liquid crystal molecules are aligned in the same direction, the rod structure and special arrangement structure of nematic liquid crystal molecules make them exhibit the characteristics of a uniaxial crystal, that is, the refractive index differs at different incidence angles along the direction of the long axis. When the incident polarized light and the long axis of nematic liquid crystal molecules are incident at an angle of ω , The beam of light can be divided into two parts, one beam of light is ordinary light (o light) with a refractive index of n_o , and another light is extraordinary light (e light) with a refractive index of n_e , which is precisely the birefringence effect of liquid crystal. Applying an electric field on both sides of the nematic liquid crystal layer, the liquid crystal molecules will reorient after the voltage

value exceeds a certain threshold, which causes the optical axis direction of the uniaxial crystal to change. This phenomenon is called the electro-birefringence effect of liquid crystals. The working principle of the pure phase LC-SLM is to use the electronic birefringence effect to realize the beam deflection through the pure phase modulation of the incident light. Thus, the LC-SLM is an ideal modulator to realize the intelligent control of a laser beam.

The SLM used in the experiment belongs to the PLUTO-2 reflection series produced by Holoeye, and the technique used for this model is liquid crystal on silicon (LCOS).

For a phase only spatial light modulator, when a voltage is applied, the liquid crystal molecules will be rotated in the direction of the electric field. If the polarization direction of the incident beam makes an angle θ with the long axis of the liquid crystal, according to the geometric vector relationship, the complex amplitude component on the x-axis and y-axis is:

$$\begin{aligned} E_x &= A \cos \theta \\ E_y &= A \sin \theta \end{aligned} \quad (3.1)$$

where A is the complex amplitude of the original polarized beam. The above is the amplitude information of the beam, For principle of phase modulation, Due to the birefringence effect of liquid crystal molecules, the refractive index of liquid crystal long axis and short axis is different, and the light can be divided into ordinary ray(o ray) and extraordinary ray(e ray), the two rays have different phase velocities in two directions, so the phase modulation can be realized by using this effect. The phase difference between o ray and e ray can be expressed as:

$$\Delta\varphi = \frac{2\pi}{\lambda} |n_{\text{eff}} - n_o| d \quad (3.2)$$

$$\frac{1}{n_{\text{eff}}^2} = \frac{\cos^2\theta}{n_o^2} + \frac{\sin^2\theta}{n_e^2} \quad (3.3)$$

where λ is the wavelength, d is the thickness of the LC layer, n_{eff} is the effective refractive index, varying with the applied electric field, n_o is the ordinary refractive index of the LC, and n_e is the extraordinary refractive index of the LC.

3.2 Holography

Based on digital computing and modern optics, the computer generated hologram (CGH) was first proposed in 1965 by Kozma and Kelly [70]. Subsequently, Lohman et al, a team working at IBM in the United States, made the first CGH recording of amplitude and phase with a computer instead of a laser, which laid the foundation for the development of CGH [71].

Based on the preliminary achievements of CGH, many researchers have put forward many kinds of CGH coding techniques. In 1967, Burch [72] made a modified off-axis reference hologram by adding off-axis reference light and increasing bias in the complex signal encoding of object light waves. The computational hologram made by this method is called a Burch-type computational hologram. This coding technique replaced the cell oriented holograms by point holograms and made this kind of computer generated holograms more attractive. In 1969, Lesem [73] proposed the phase diagram coding technique, the advantages of this coding technique lie in its high diffraction efficiency and coaxial reproduction. In 1970, Lee [74] made a computational hologram with another new coding technology, which divided the sampling unit into four small units and then encoded the complex value of the sampling point with these four small units. This holographic coding method proposed based on the effect of indirect phase is called fourth-order indirect phase coding. Through analysis, Kamperer et al. [74] found that Lee-type CGH is one of the ways to correct off-axis reference light coding. Burckhardt later proposed a novel coding method for Lee-type CGH in order to simplify the encoding method of holograms based on the indirect phase effect. [75].

After 1980, along with the emergence of various new technologies, CGH technology began to develop rapidly. Holograms could only be recorded with holographic dry board before, the real-time and repeatability were poor. However, with the introduction of modern spatial light modulator technology, the computer-coded CGH can be output to a spatial light modulator (such as spatial acousto-optic modulator, liquid crystal spatial light modulator, digital micromirror device, etc.), making it possible to realize real-time display based on the CGH technology.

3.3 Vortex beam production method

So far, computational holography is the simplest and most effective method to generate vortex beams. In 1990, some groups began using diffractive optical elements to create optical vortices. Soskin and his collaborators realized that the diffraction grating with a central edge dislocation had optical singularities in its first-order diffraction beam [76–78], and successfully obtained optical vortices of ± 1 order. In order to obtain higher-order Bessel beams, Heckenberg et al. [79] first reported the use of computational holography to generate doughnut shaped hollow beams in 1992. In 1996, Paterson et al. [80] designed the finite aperture rotating prism type computational holography to generate two approximate high-order Bessel beams, developed a new theoretical analysis method to describe the principle of producing high-order Bessel beams, and explained their experimental results.

Computational holography combines multiple disciplines, including computer science technology, optical theory, and optical holography technology. Among them, the grating made by the holographic method has high diffraction efficiency, which improves the success rate of making vortex beams. Among

them, the diffraction image is usually taken from the first order diffraction beam. The computational holography method for vortex beam generation mainly introduces a phase singularity in the incident Gaussian beam, and the singularity is represented by a misaligned grating in the center of the hologram. This method of generating vortex beams consists of three parts: the first step is to calculate the mathematical expressions of the desired order of vortex beams, and use computer software to program the mathematical formulas to generate two-dimensional computational holograms; the second step is to make a hologram film with the generated computational hologram according to a certain ratio; and the third part is to irradiate the plane wave with the same phase and amplitude of the incident plane wave onto the hologram film to generate a vortex beam.

For the production of a holographic fork grating, in the experiment, a plane wave and a vortex beam with orbital angular momentum are interfered and superimposed to form a two-dimensional computer hologram, which records the amplitude and phase information. Suppose the electric field expression of a plane wave beam is:

$$E_1 = A_1 \exp(ikx \sin \alpha +iky \cos \alpha) \quad (3.4)$$

The expression of the vortex beam propagating along the optical axis z is:

$$E_2 = A_2 \exp(i\ell\theta) \quad (3.5)$$

where A_1 and A_2 are the amplitude of the light wave, and ℓ is the orbital angular momentum of the vortex beam. The light intensity distribution of the interference and superposition of these two light waves on the $z = 0$ plane is:

$$I = (E_1 + E_2)(E_1 + E_2)^* = A_1^2 + A_2^2 + 2A_1A_2 \cos(\ell\theta - kx \sin \alpha) \quad (3.6)$$

If both vortex light wave and plane wave are light waves of unit amplitude, that is, $A_1 = A_2 = 1$, then the light intensity can be expressed as:

$$I = 2 + 2\cos(\ell\theta - kx \sin \alpha) \quad (3.7)$$

We use Matlab software to achieve our goal. By changing ℓ value, we can get fork-shaped gratings of different order topological charges, as shown in Fig. 3.1. In the Fig. 3.1, (a) and (b) are the forked gratings of order 1 and order 2 respectively, namely the first and second-order interference patterns. In Fig. 3.1 (a), an additional bright stripe appears in the middle and upper part, resulting in a fork structure in the middle. Fig. 3.1 (b) for vortex beam of order 2, two additional bright stripes appear in the middle, and so on, so N additional bright stripes appear for the generation of vortex beams of order N . Fig. 3.1(c), Fig. 3.1(d) for fork-shaped gratings of order 0.5 and 0.8, which are non-integer,

will have a fault in the middle, but the fork-shaped structure in the center does not change. It can be known that the number of center dislocation of hologram is topological charge ℓ , with its light and dark fringes determined by $\ell \frac{\varphi}{\pi} = n + \frac{2r}{\Lambda} \cos \varphi (n = 0, \pm 1, \pm 2 \dots)$, where Λ is the grating constant, r is the distance from the center point of the grating, and φ is the Azimuthal Angle.

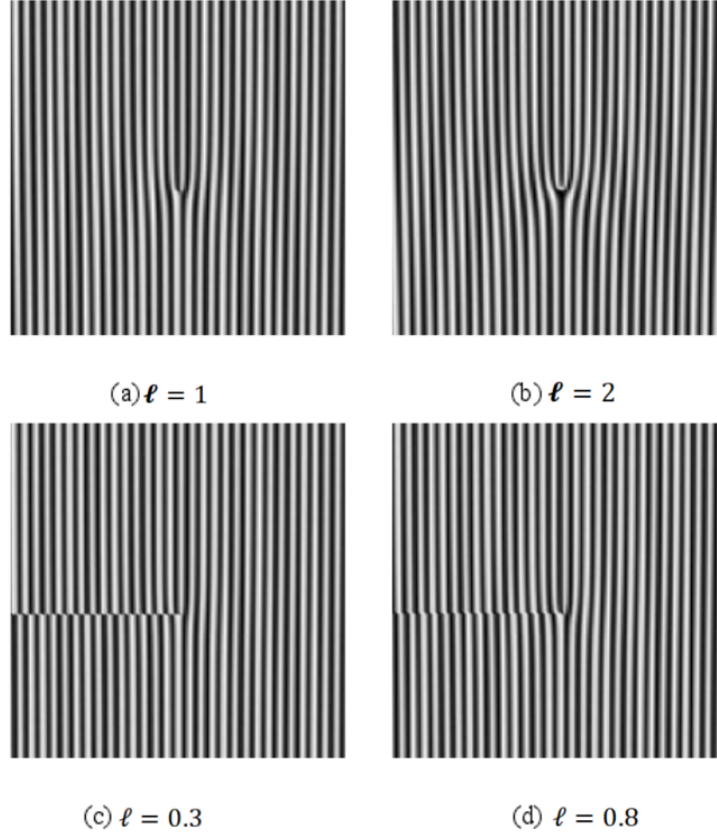


Figure 3.1: Forked gratings with different order topological charges, black maps to 0 grayscale and white maps to 255 grayscale

With the development of technology, spatial light modulator (SLM) can be used to conduct spatially distributed modulation of light waves, and the designed phase information map can be directly displayed on pure phase SLM, and optical vortices can also be generated by irradiating. Curtis and Grier [81, 82], for example, uses this method to obtain vortex beams. Using this device they also produced a deformable optical vortex [82].

Currently, generating optical vortices on SLM using computational hologram display has become the most commonly used method in the laboratory. Using this method, it is very convenient to control the beam parameters such as the

topological charge of the vortex and adjust its spatial distribution dynamically and in real time by just controlling the phase hologram displayed on SLM via a computer.

3.4 Beam deflection by blazed grating

As illustrated in Fig. 3.2, a beam can be deflected if it passes through an optical prism or the equivalent.

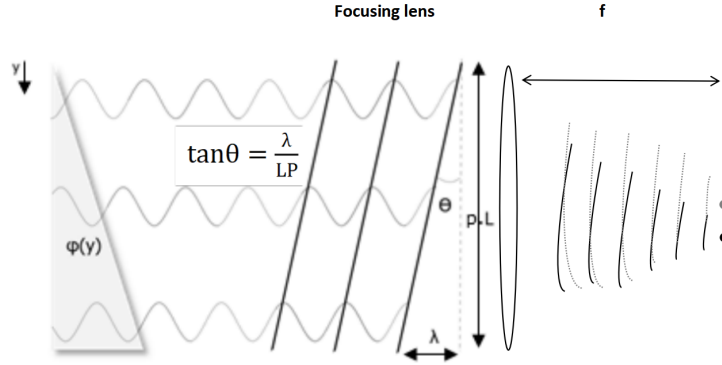


Figure 3.2: Introducing linear phases change on the incoming plane wave causes a tilt on its direction. Consequently, it produces a 1D transverse shift of the spot at the focal plane of the lens. when phases change linearly along the y-axis, the optical wavefront is tilted by an angle, θ , due to a linear phase shift, L is the period of the phase, producing a difference of λ on the optical path. P is the pixel width. The phase modulation of SLM can be equivalent to that of prism.

Taking a grating hologram as an example, it is equivalent to that of a prism if the wave front is modulated by a linear ramp within each grating element, with a maximum amplitude 2π . This is a blazed grating. The condition for such a tilting angle also coincides the condition for the 1st order diffraction beam, hence the efficiency for the 1st order diffraction is also maximized. This is important as we will use the 1st order diffraction pattern to encode the vortex information.

As shown in Fig3.2, according to the trigonometric function, the beam deflection angle θ can be calculated by Eqn. 3.8

$$\theta = \arctan\left(\frac{\lambda}{LP}\right) \quad (3.8)$$

where λ is the wavelength of the incident light, L is the width of each pixel in SLM, and P is the number of pixels in a period of the blazed grating.

In this case, adjusting the pixel number of the blazed grating element, P , allows the beam steering, as shown in the Fig. 3.3.

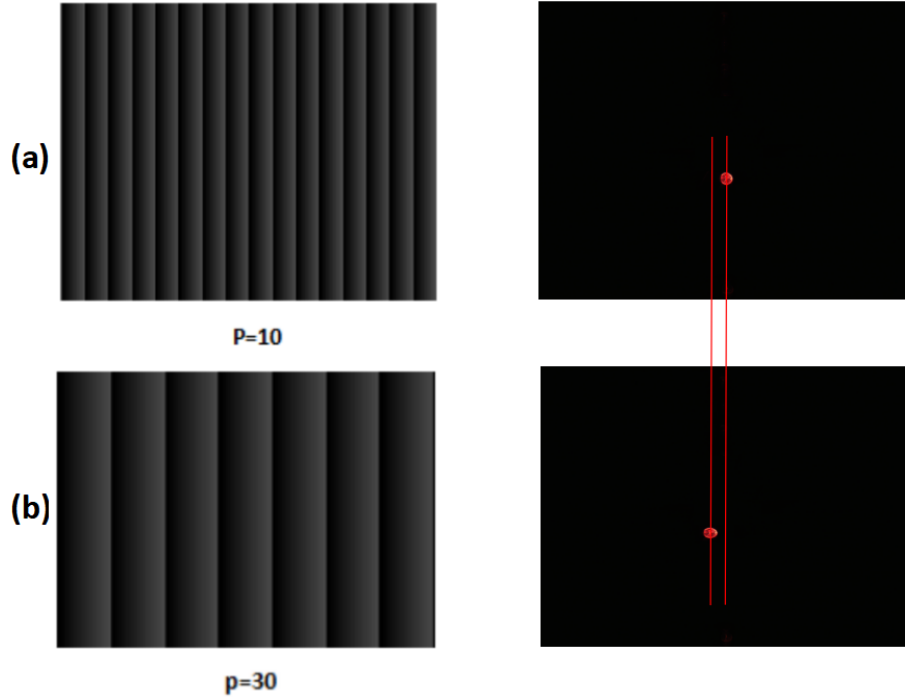


Figure 3.3: (a) and (b) represent the blazed grating(left) with different pixel periods and its corresponding diffraction pattern(right), respectively, and the red line clearly indicates the steering of light in the horizontal direction. order topological charges, black maps to 0 grayscale and white maps to 255 grayscale

3.5 Reconstruction algorithm for ptychography

The introduction of the basic concept of image stacking demonstrated that it is essentially a phase recovery method, and the stacked iterative algorithm is essentially a phase recovery algorithm, but it is distinct from the traditional phase recovery algorithm [83]. In this section, two commonly used stack imaging reconstruction algorithms are introduced: the conventional stack imaging algorithm(PIE) and the extended stack imaging algorithm(ePIE) [83, 84].

3.5.1 PIE algorithm

PIE algorithm works by moving the illumination probe so that the beam scans the region of interest of the sample, and record the far-field diffraction pattern corresponding to each probe. The position of the probe following each movement of the probe is determined. Fig. 3.4 presents the block diagram of the algorithm, and this derivation follows Ref [83].

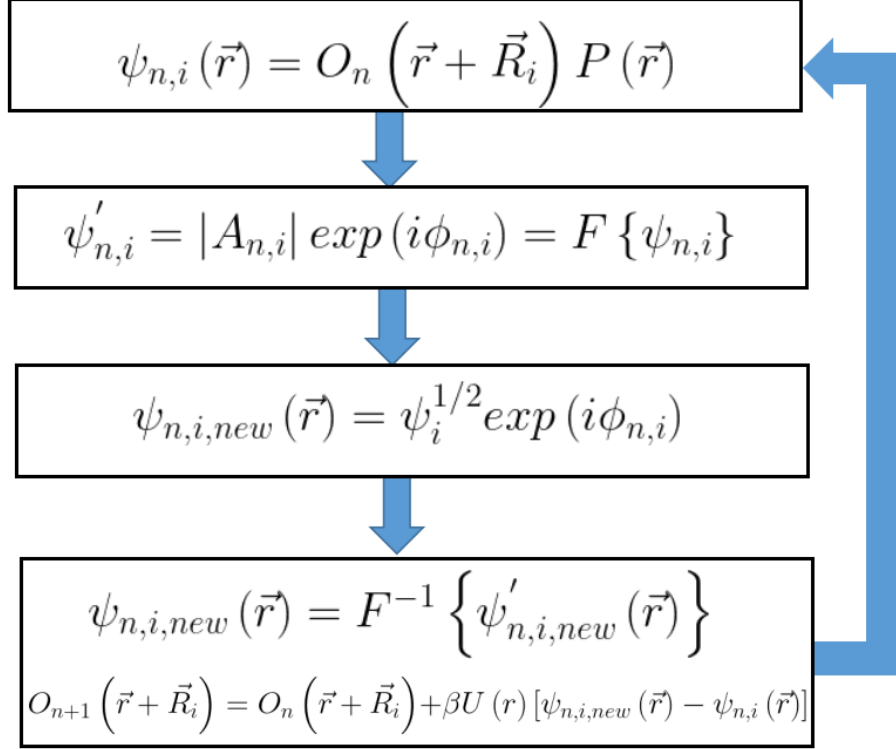


Figure 3.4: Block diagram of PIE algorithm

The algorithm first requires one to guess the initial value of an object function $O_n(\vec{r} + \vec{R}_i)$. After the light wave passes through the object with the complex amplitude, the transmitted wave function is the product of the object function and the probe function, $P(\vec{r})$:

$$\psi_{n,i}(\vec{r}) = O_n(\vec{r} + \vec{R}_i) P(\vec{r}) \quad (3.9)$$

where, n represents the index of the current iteration, \vec{r} is the corresponding objective plane coordinate vector, i is the number of probes at different positions, and \vec{R}_i represents the displacement vector from the initial probe position to the position of the i_{th} probe: The far-field diffraction complex amplitude obtained on the output plane is:

$$\psi'_{n,i} = |A_{n,i}| \exp(i\phi_{n,i}) = F\{\psi_{n,i}\} \quad (3.10)$$

where F stands for Fourier transform.

In the iteration, the amplitude distribution, $|A_{n,i}|$, is updated by the square root value $\psi_i^{1/2}$ of the strength pattern of the far field diffraction pattern recorded

in practice, while the phase of Eqn. 3.10 remains unchanged. Then the complex amplitude distribution of the new output surface is obtained as

$$\psi_{n,i,new}(\vec{r}) = \psi_i^{1/2} \exp(i\phi_{n,i}) \quad (3.11)$$

The modified output complex function is inverse transformed via Fourier transform, returned to the object space:

$$\psi_{n,i,new}(\vec{r}) = F^{-1} \left\{ \psi'_{n,i,new}(\vec{r}) \right\} \quad (3.12)$$

where F^{-1} stands for inverse Fourier transform, and the object function is updated accordingly:

$$O_{n+1}(\vec{r} + \vec{R}_i) = O_n(\vec{r} + \vec{R}_i) + \beta U(\vec{r}) [\psi_{n,i,new}(\vec{r}) - \psi_{n,i}(\vec{r})] \quad (3.13)$$

With the updated function:

$$U(\vec{r}) = \frac{P(\vec{r})}{\max(|P(\vec{r})|)} \frac{P^*(\vec{r})}{|P(\vec{r})|^2 + \alpha} \quad (3.14)$$

Among them, α and β are constants, and their values will affect the convergence speed and stability of the algorithm. $|\beta| \leq 1$ is the feedback coefficient, and the typical range of the values is $\beta \in [0.9, 1]$; α prevents the algorithm from being unable to proceed if $|P(\vec{r})|^2$ is zero. If the probe function is normalized, it is more appropriate for α to take the value of 0.001. The part $|P(\vec{r})| / \max(|P(\vec{r})|)$ of the updated function ensures that the object is mainly changed at positions where the probe has its highest magnitude. The part $P^*(\vec{r}) / |P(\vec{r})|^2$ removes the initial multiplication with the probe function in Eqn.3.9 from the exit wave. [85].

One then use the updated object function as the new guess for the next iteration.

To calculate the similarity between the reconstructed image and the original image, correlation coefficient C_o and mean square error (MSE) are quantitative indicators used .

C_o is defined as follows:

$$C_o(f, f_0) = \text{cov}(f, f_0) (\sigma_f, \sigma_{f_0})^{-1} \quad (3.15)$$

where f and f_0 are the complex amplitudes of the decrypted image and the original encrypted image respectively, $\text{cov}(f, f_0)$ is the cross-covariance of f and f_0 , and σ_f and σ_{f_0} are the standard deviations. To evaluate the decryption quality, phase relation values C_{0A} and $C_{0\varphi}$ of amplitude and phase should be calculated respectively.

MSE is defined as:

$$\text{MSE} = \frac{1}{M \times N} \sum_{i=1}^M \sum_{j=1}^N |f'(i, j) - f(i, j)|^2 \quad (3.16)$$

where $M \times N$ represents the size of the object, $f'(i, j)$ and $f(i, j)$ represent reconstructed image and original image respectively.

The closer C_o value gets to 1, the closer the distribution of the two image functions are. The smaller the value of MSE, the more similar the distribution of the two functions.

If C_o or MSE meets the expected standard, then the recovered complex function is the expected reconstructed image function. If C_o or MSE does not meet the expected criteria, the complex amplitude of this recovery is taken as the initial value for the next iteration. Iteration continues until the decrypted image meets the requirements.

The PIE algorithm is characterized by the fact that the probe function is known and that iteration and guessing occur simultaneously. In practice, however, neither the probe function nor the probe position can be determined with any degree of precision.

3.5.2 ePIE algorithm

The ePIE algorithm is similar to the PIE algorithm. The difference is that the probe function is also updated at each iteration [86]. The initial output function is the product of the guessed probe function and the object function [87]. Due to the fact that neither the probe function nor the moving position of the probe can be accurately determined, so the ePIE algorithm updates the probe function and the object function at the same time during each iteration. The update of the probe function is similar to the update of the object function:

$$P_{n+1}(\vec{r}) = P_n(\vec{r}) + \beta \frac{O_n(\vec{r} + \vec{R}_i)}{\max(|O_n(\vec{r} + \vec{R}_i)|)}$$

$$\frac{O_n^*(\vec{r} + \vec{R}_i)}{|O_n(\vec{r} + \vec{R}_i)|^2 + \alpha} [\Psi_{n,j,new}(\vec{r} - \Psi_{n,j}(\vec{r}))] \quad (3.17)$$

The updated probe function and object function are taken as the initial values for the next iteration. Compared with PIE pressure algorithm, The ePIE algorithm has a faster convergence speed.

Chapter 4

Calibration of SLM

The spatial light modulator is a new programmable optical element. This instrument mainly uses liquid crystal to realize the continuous modulation of the phase of light wave. Therefore, the spatial light modulator is a very powerful instrument in the laboratory and has a wide range of applications in adaptive optics, holographic optics, high-resolution imaging and other optical fields. However, the LC-SLM-based liquid crystal material has its own characteristics. In addition, dispersion will also affect the LC-SLM experiment as different wavelengths of incident light have different refracting effects on the liquid crystal molecules. Therefore, the LC-SLM needs to be calibrated for the working wavelength of the laser used.

In order to obtain the phase modulation range of LC-SLM more accurately and perform calibration, A binary grating is used firstly to measure the phase modulation range of the LC-SLM, and then a bowman blazed grating is used to perform phase calibration. The method of measuring the phase modulation range is mainly to load a grating image with the required gray level change onto the LC-SLM, then the beam intensity of the 0th order diffraction beam spot is detected and a curve of beam intensity dependence on the gray scale change is plotted. This is compared with the beam intensity value of the corresponding gray level. In that way, we measured the phase modulation range. After the phase modulation range is determined, the phase calibration is mainly performed through the bowman grating to obtain the diffraction pattern under different contrast, and finally the best contrast can be received to achieve the best phase modulation.

4.1 Construction of experimental platform

According to the experimental requirements, the experimental platform shown in Fig. 4.1 was built. The laser with a wavelength of 632.8 nm realized a 4.5-fold beam expansion through lens 1 with a focal length of 20 mm and lens 2 with a focal length of 90 mm. The beam polarization was adjusted by rotating the laser

tube and polarizer 1 to ensure the polarized beam is along the vertical direction which is the default direction of LC molecules, The beam is then led through the beam splitter (BS) to fill the SLM's effective LCD . The beam is reflected by the LC-SLM and the BS prism and then is focused onto the detection surface of the CCD camera through a lens 3 with a focal length of 30 mm.

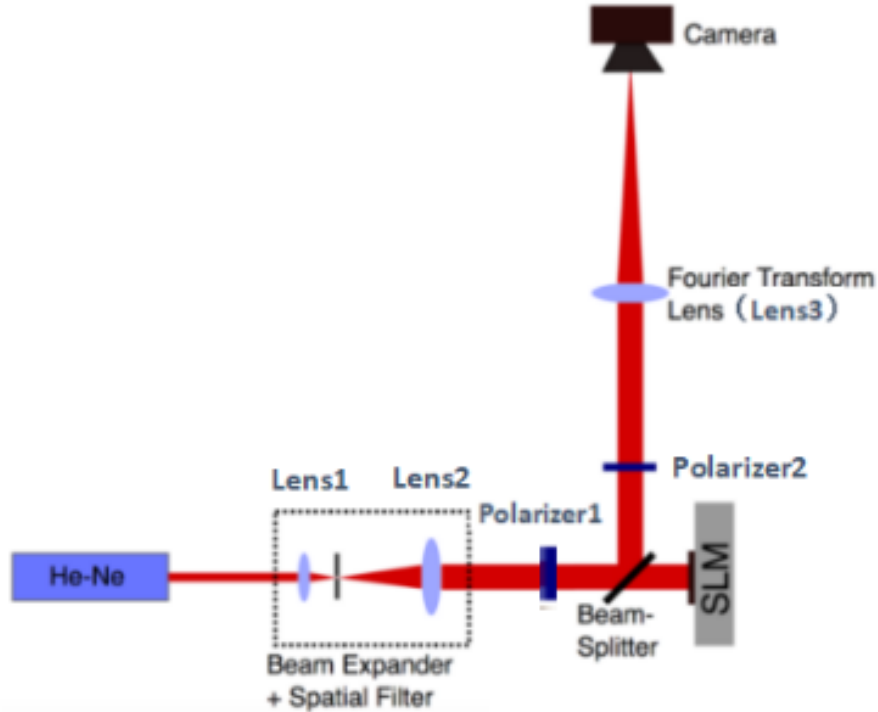


Figure 4.1: The optical system used in the experiment is mainly used to measure the far-field diffraction pattern produced by the hologram displayed on the SLM by a computer. The beam from the laser is expanded by the lenses 1 and lens 2, being processed into polarized light by a polarizer and modulated by SLM, and then Fourier transformed by a lens 3. Finally, using the camera in the Fourier plane of the SLM to measure the diffraction pattern

4.2 Determination of phase modulation range

This experiment uses a version of PLUTO-VIS-016c from Holoeye company with a resolution of 1920×1080 , which is mainly based on electrically controlled nematic liquid crystals to adjust the wavefront of the incident wave. This version

of the SLM has a pixel pitch of $10\ \mu\text{m}$, so it can achieve high resolution and capable of a large deflection angle. The laser model used in this experiment is HNLS008L self-contained HeNe Laser, and its wavelength is $632.8\ \text{nm}$. The purpose of this section is to obtain the phase response of this SLM. To be compared with the actual result of the experiment, it is known through the manual [88] that the SLM can achieve a phase modulation of 5.3π at a wavelength of $623\ \text{nm}$.

4.2.1 Phase grating diffraction characteristics

According to Fourier optics [89], when the two-dimensional phase grating placed in front of the lens is illuminated by coherent light, the beam intensity distribution on the focal plane of the lens is equal to the square modulus of the Fourier transform of the phase grating in front of the lens [89]. We loaded a black and white grating image onto the SLM, as shown in Fig. 4.2. The black part of the phase delay is 0, the white part of the phase delay is a variable value. We place the SLM in front of the lens and illuminated it with a coherent light. At this time, the action of the SLM is equivalent to a two-dimensional phase grating, so that the beam intensity distribution of the diffraction spot shown in Fig. 4.3 is obtained at the focal plane behind the lens.



Figure 4.2: One element of the binary grating

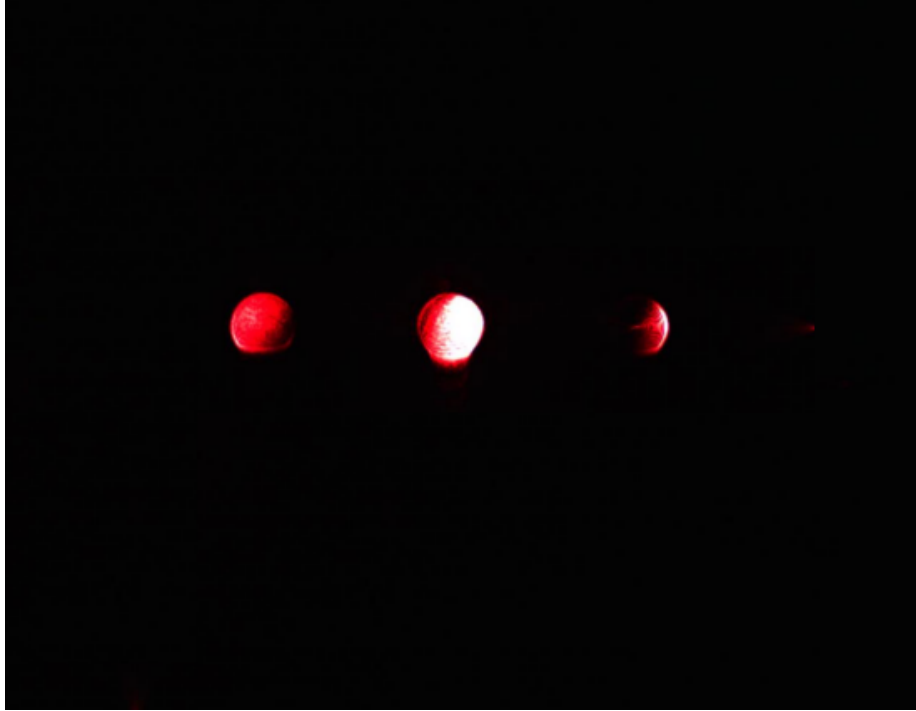


Figure 4.3: Diffraction pattern due to the binary grating of Fig .4.2

Changing the phase contrast of the black and white grid of the binary grating (equivalent to changing the phase retardation of the black grid), the beam intensity of the zero-order diffraction spot (central spot) located on the rear focal plane of the lens will also change accordingly. In this way, the phase contrast of the binary grating loaded on the SLM can be obtained by measuring the intensity of the zero-order diffraction spot behind the lens.

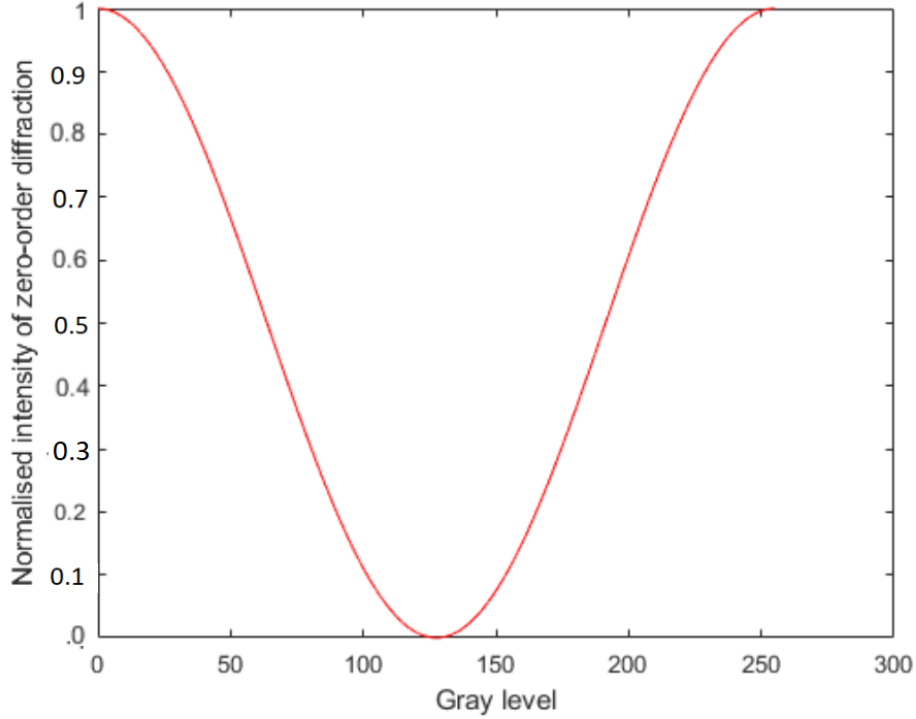


Figure 4.4: Relationship between gray level and normalised intensity of zero-order diffraction spot

In fact, we need to normalize 0-order light, and the normalization process is:

$$I_n = I_0/I_t \quad (4.1)$$

Where I_n is the normalized intensity, I_0 is the optical diffraction intensity of order 0, and I_t is the intensity of the reference beam spot, which is the intensity of the 0-order beam spot without grating structure.

Through calculation, the relationship between the intensity of the zero order diffraction spot and the contrast of binary phase grating is:

$$I = (1 + \cos\Delta\varphi)/2 \quad (4.2)$$

Where I is the normalized intensity of the zero-order diffraction spot. $\Delta\varphi$ is the phase contrast of the binary phase grating. From the above discussion, the phase contrast of the binary phase grating in front of the lens can be obtained by measuring the light intensity of the zero-order diffraction spot on the focal plane behind the lens. The phase delay represented by the binary grating black lattice is then obtained. According to the corresponding relationship between the phase delay and the gray level of the computer can be obtained, and the phase modulation characteristics of SLM can be obtained.

4.2.2 Experimental set up

As shown in Fig. 4.1, the 632.8 nm laser is coupled into the beam expander, and then it is collimated by the collimating lens through the beam expander, and then enters the polarized beam into splitting prism, and is divided into two beams of linearly polarized light. The polarization direction of the transmitted beam is parallel to that of the liquid crystal molecules of the LC-SLM, that is, the polarization direction of the transmitted light is the same as that of the light modulated by the LC-SLM. A binary hologram is loaded into the LC-SLM by computer. The size of each lattice is $18 \text{ pixels} \times 18 \text{ pixels}$. The gray level of white grid is 255, and the gray level of black grid is variable value. The LC-SLM is equivalent to a variable two-dimensional phase grating. After being illuminated by laser, we take the 0 order beam spot as the wanted spot, the image shown in Fig. 4.5. The 0 order diffraction spot of binary grating is on the left, and the reference spot is on the right. Followed the eqn.4.1, after the image is collected, the intensity of zero-order diffraction spot is divided by the intensity of reference spot which is the intensity of the 0-order beam spot without grating structure, and the obtained result is taken as the normalised intensity value of zero-order diffraction spot, so as to standardize the data quantification.

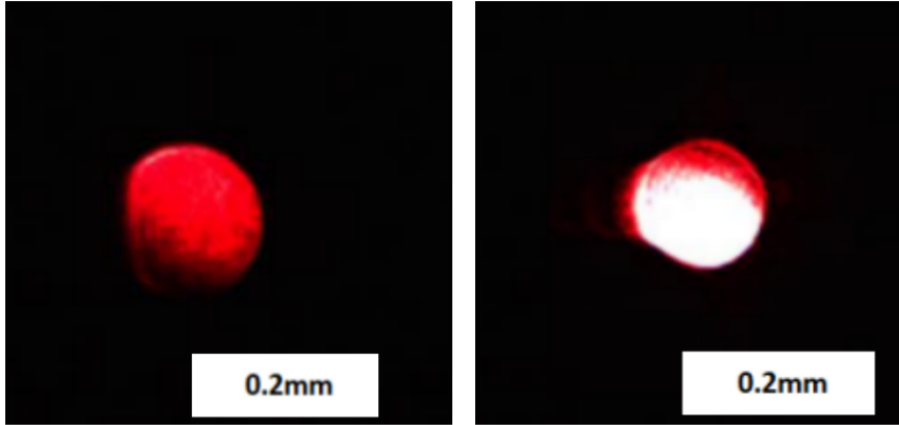


Figure 4.5: The 0-order diffraction beam spot of binary grating (left) and the reference 0-order beam spot without grating structure(right).

4.2.3 Experimental result

In order to obtain the accurate phase modulation range, the diffraction pattern for both horizontal and vertical polarizations of the incident beams were measured respectively. Followed the eqn.4.1, the ImageJ software can used to analyze and record the different zero-order beam spot captured by the CCD camera.

Vertical polarization

When the incident beam polarization is consistent with the long side direction of the SLM micro display panel, the incident polarization state can be basically not affected, and the purpose of changing only the phase can be achieved.

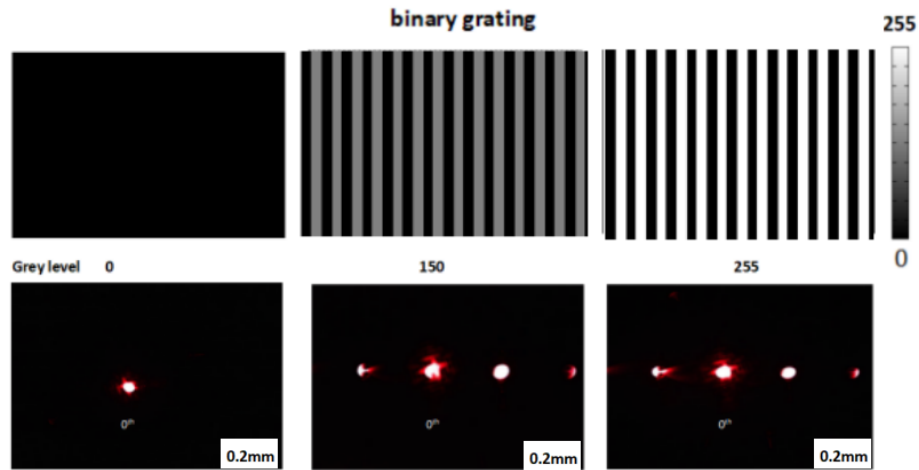


Figure 4.6: Longitudinal strip binary grating and evolution of the experimental intensities of the zero-order beam spots when increasing the gray value of the 'white' strips.(for an incident beam with vertical polarization)

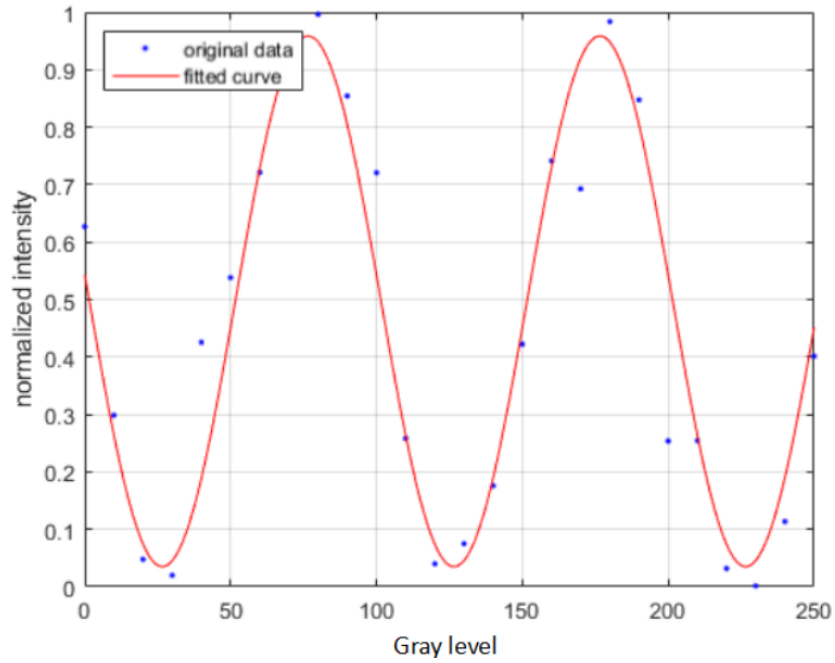


Figure 4.7: The normalized 0th order diffraction beam (vertical polarization) as a function of the maximum gray level of the binary grating, together with a curve fitting of the data using $a + c\cos(\text{graylevel})$.

Horizontal polarization

In order to compare with the experimental data for the vertical incident polarization, data were obtained by adjusting the incident polarization of the laser to the horizontal state.

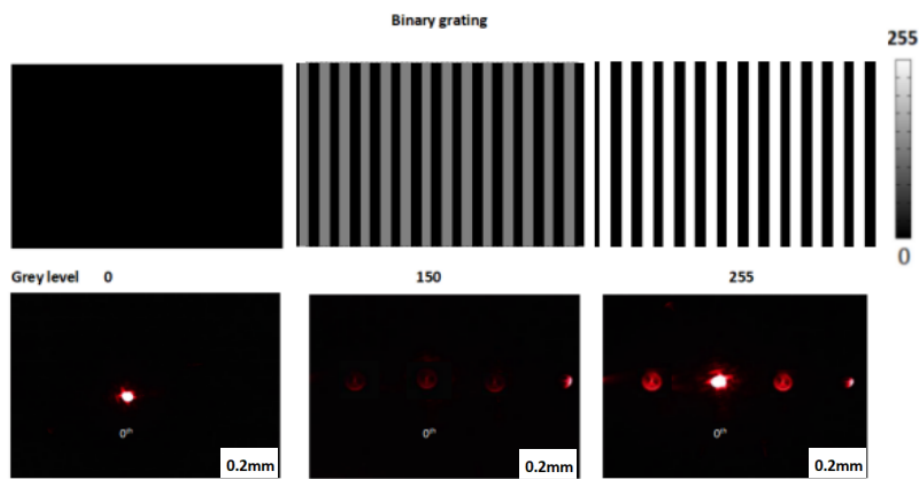


Figure 4.8: Longitudinal strip binary grating and evolution of the experimental intensities of the zero-order beam spots when increasing the gray value.(for an incident beam with horizontal polarization).

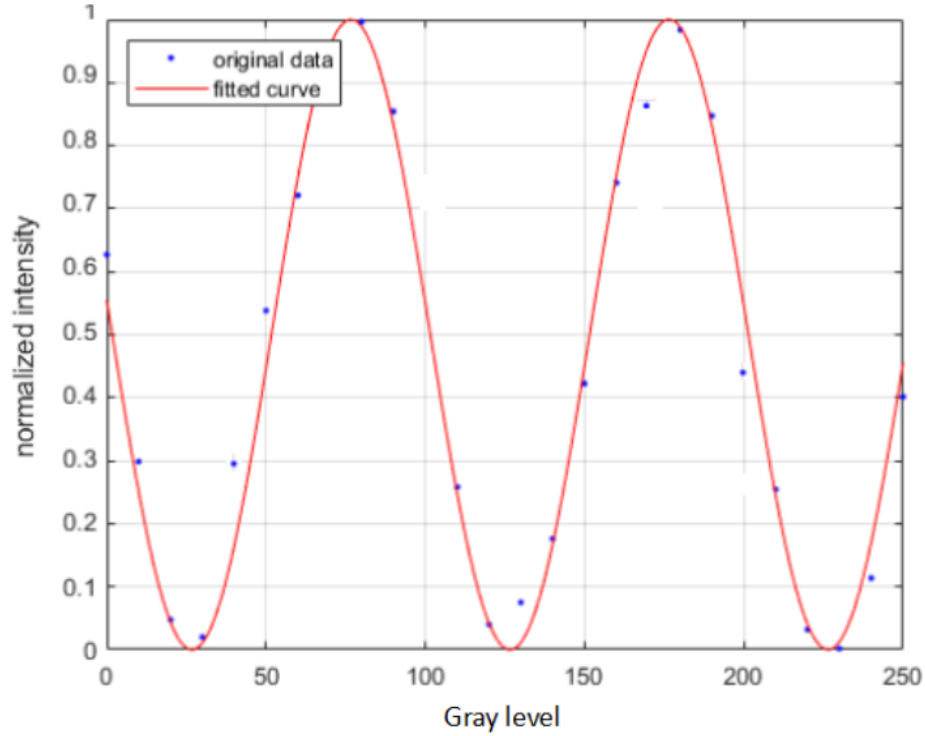


Figure 4.9: The normalized 0th order diffraction beam(horizontal) as a function of the maximum gray level of a binary grating, together with a curve fitting of the data using $a + c \times \cos(\text{graylevel})$.

4.2.4 Results and Analysis

From the above experimental results of horizontal and vertical incident polarization, it can be seen that the general trends of the two results are similar, but there are still some differences, which are mainly due to the birefringence effect of the liquid crystal. For different polarization states, liquid crystals have different optical characteristics, that is, for a spatial light modulator, when the polarization state of the incident beam is consistent with the direction of the long axis of the liquid crystal, phase-only modulation can be achieved efficiently, and when the polarization state is consistent with the direction of the short axis of the liquid crystal, phase modulation cannot be achieved easily. From the experimental images, we can see that the incident beam still achieves phase modulation when polarized horizontally. This is mainly because it cannot be fully guaranteed that the incident polarization is perpendicular to the short axis of the liquid crystal. For above analysis, The comparison between the experimental results of horizontal polarization and vertical polarization also explains why the phase modulation can be obtained in the case of horizontal polarization

and the phase modulation is similar, but the intensity of the diffraction beam is weak relative to the vertical incident polarization.

Through the above analysis, we fitted the corresponding relationship between the horizontal and vertical incident polarization phases, and finally take the average of the two relationships, and then the phase modulation curve of the SLM can be obtained.

According to the data of vertical polarization and horizontal polarization, the intensity value of the zero-order diffraction spot corresponding to each gray level can be obtained, then the phase delay value corresponding to the intensity value can be calculated. Finally, the phase delay corresponding to each gray level can be deduced.

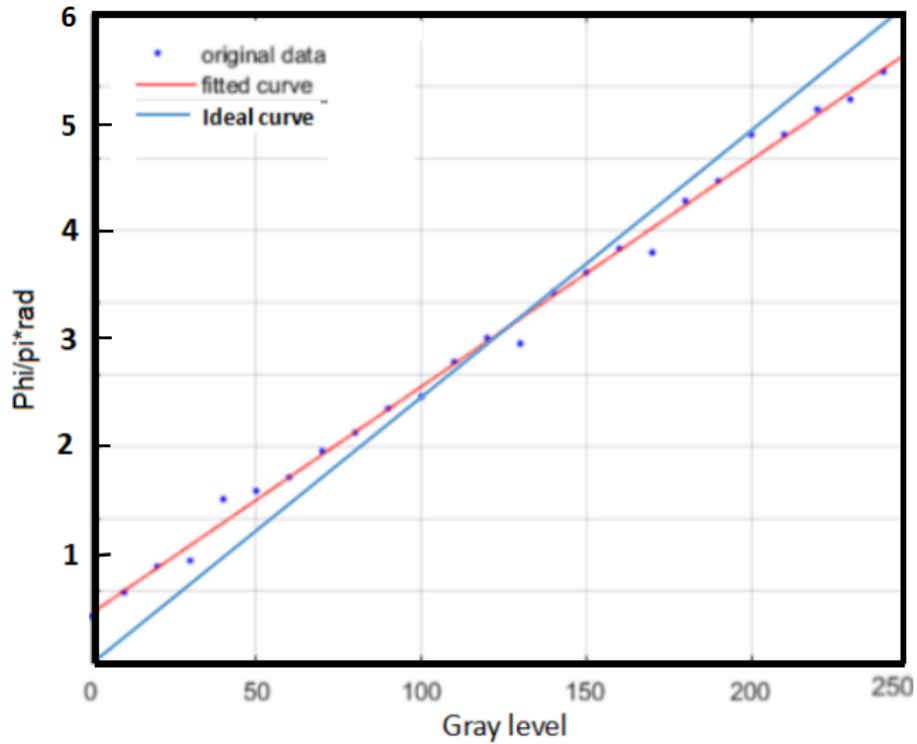


Figure 4.10: The phase response curve (phase change vs.maximum gray level).

According to Fig. 4.10, comparison with the ideal curve with a modulation range of 6π , the linear relationship between gray value and phase modulation obtained in the experiment is not perfect, and there is a certain gap between the slope and the ideal curve, so it needs to be corrected.

4.3 SLM phase modulation calibration

In reality, because each pixel of the spatial light modulator cannot achieve the ideal phase modulation, this will reduce the overall diffraction efficiency of the beam. An effective method introduced by Bowman is to adjust the blazing function to improve the phase modulation effect which shown as Fig. 4.11.



Figure 4.11: (a) A set of ramps wrapped at 2π . The x variable represents one spatial coordinate on the SLM. (b) A real SLM can reach a maximum value of the phase ϕ_{max} which is different from 2π . (c) By changing the contrast, it is possible to obtain a phase-ramp which is as similar as possible to the ideal one. Figure courtesy of [6]

As shown in Fig.4.11(c), A way to improve the intensity of the shifted spot is to modify the phase for each pixel. In order to do this, we increase the slope of each ramp to make the ramp of phase modulation as similar as possible to the ideal one in Fig.4.11(a), Thus the optimal phase modulation curve is obtained, as shown below:

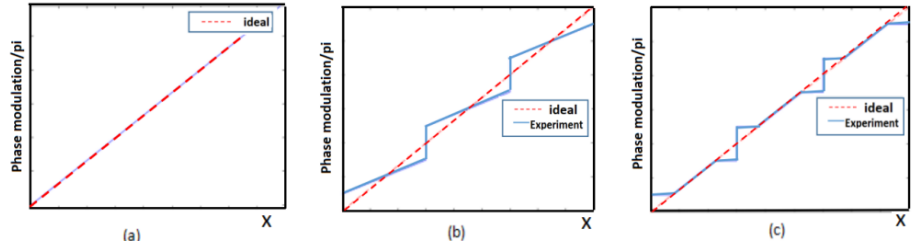


Figure 4.12: The x variable represents one spatial coordinate on the SLM. (a) The phase modulation that an ideal blazed grating can achieve. (b) A experimental SLM does not produce the desired unwrapped phase. (c) By changing the contrast, it is possible to obtain an unwrapped phase which is as similar as possible to the ideal one.

As illustrated in Fig. 4.11, by changing the contrast, we can achieve change the curve slope of the relationship between phase modulation and x value, thus, to make the actual curve as similar as possible with the ideal one. For SLM, phase modulation is controlled by gray value, so we can change the contrast through change the slope of the relationship between the gray value and x value. The relationship diagram should look like Fig. 4.13:

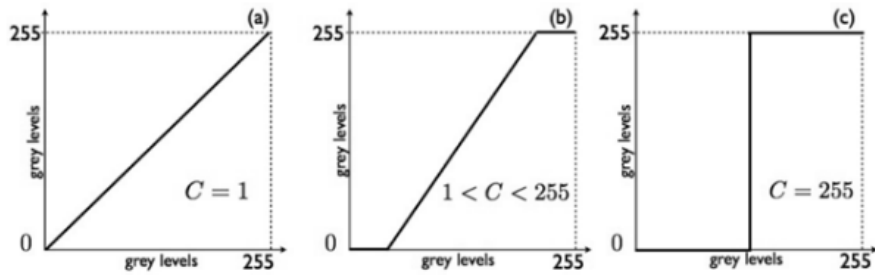


Figure 4.13: By adjusting the contrast, it will affect the hologram sent to the SLM. (a) Ideal situation with $C = 1$. (b) By increasing the contrast we increase the number of pixels that will be black or white on SLM (c) When $C = 255$ every pixel must be black or white, no matter what hologram we send into the SLM, so we have a binary hologram

Follow the above discussion, the Bowman blazed grating is used to obtain the best diffraction efficiency. For one element and the whole of Bowman blazed grating, the designs for different contrast parameters should look like as Fig.4.14 and Fig.4.15:

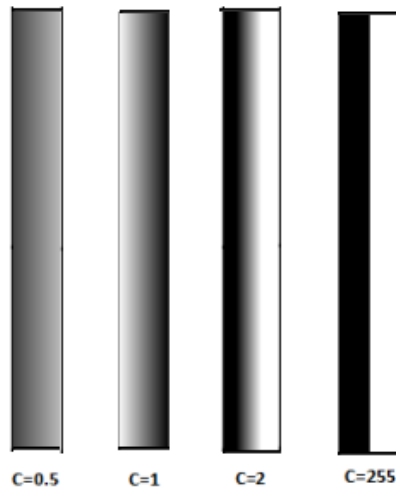


Figure 4.14: One element of Bowman blazed grating under different contrast

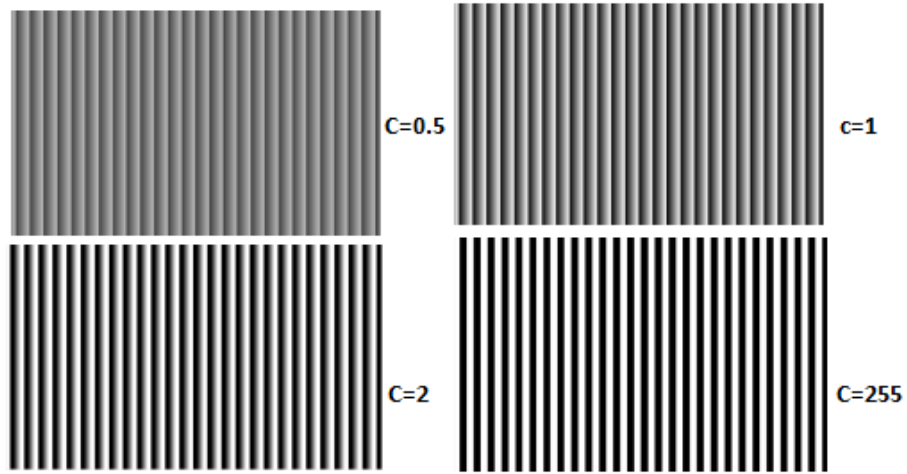


Figure 4.15: Bowman blazed grating under different contrast

4.3.1 Experimental result

By loading the SLM with the grating as shown in the Fig. 4.15 above, diffraction patterns under different contrast values can be obtained. Then, the intensity distributions of the diffraction spots are measured and normalized with the light spot of the grating when $C = 0$ as the reference (i.e. no grating structure), and the following data can be obtained.

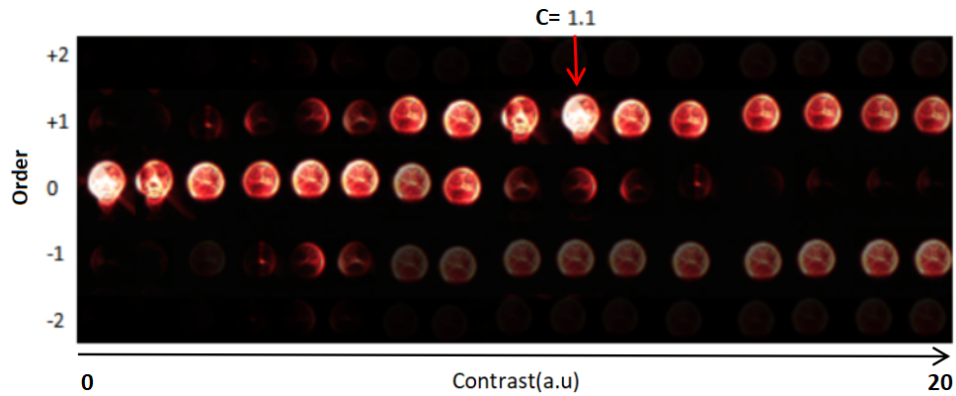


Figure 4.16: The diffraction patterns (vertically aligned) due to Bowman Blazed Grating as a function of the contrast values. The patterns were recorded at a defocus to accommodate the the finite dynamical range of the recording CCD camera.

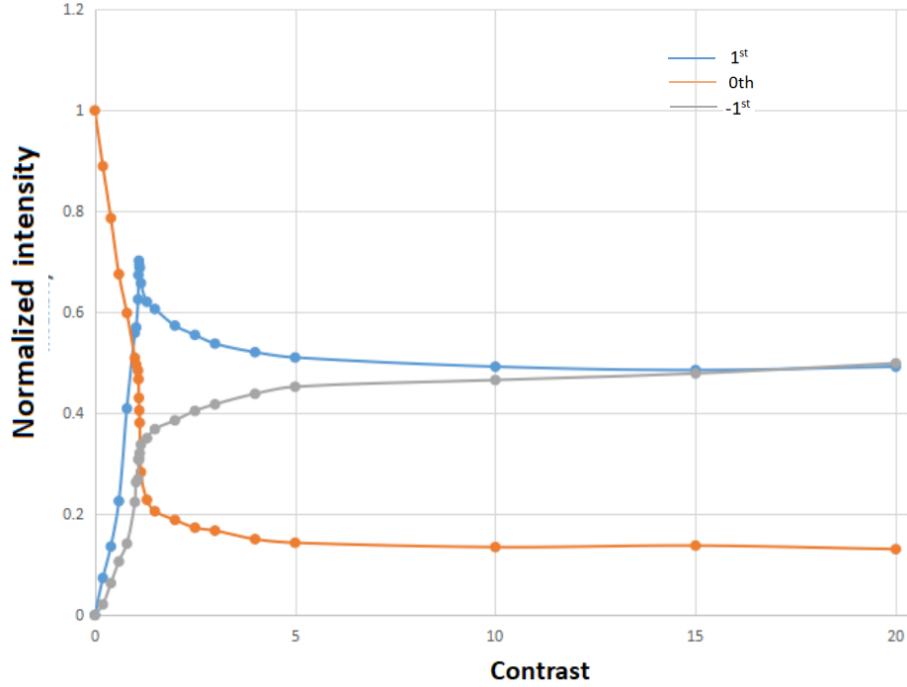


Figure 4.17: Evolution of the experimental intensities of the zero and ± 1 orders spots when increasing the contrast (normalized against the 0th order beam without diffraction grating contrast, plotted as a function of the contrast parameter.)

By analysing diffraction patterns for different values of the parameter C as shown in Fig.4.16, we can measure the zero-order light intensity and the 1st and 2nd order light intensities under different contrast levels (see Fig.4.17). We found out that the optimal contrast for our SLM was $C_{opt} = 1.1$ corresponding to a ratio between the intensities of order 1 and 0 of about 2.8. The same ratio without correction was 1. Thus, we found that the optimal contrast on the SLM is 1.1.

4.4 Combination of the two methods

In order to make the phase modulation curve of the spatial light modulator possibly similar to the phase modulation with an ideal phase of 6π , we can compare the relation between the binary grating and the blazed grating.

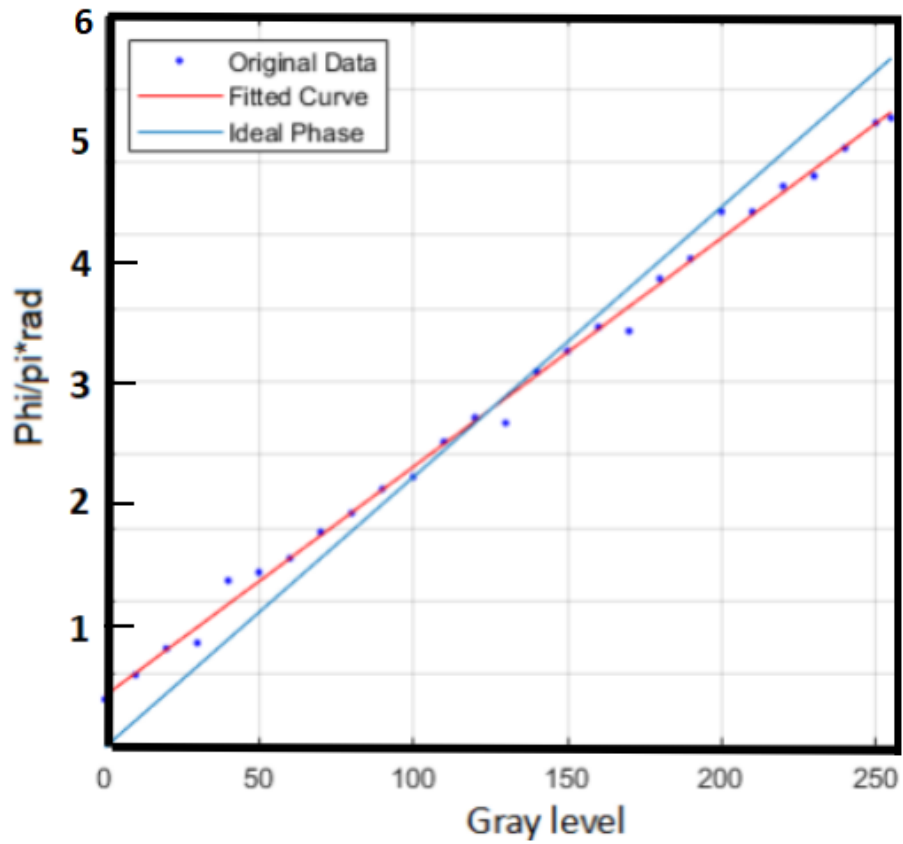


Figure 4.18: The phase modulation curve of the spatial light modulator (red curve drawn through experimental data). Also plotted is the idealised spatial light modulation curve (blue).

As shown in the Fig. 4.18, the red line is the actual relationship between phase modulation and gray level obtained through Binary Grating, while the blue line is an ideal phase modulation curve with a phase modulation of 6π .

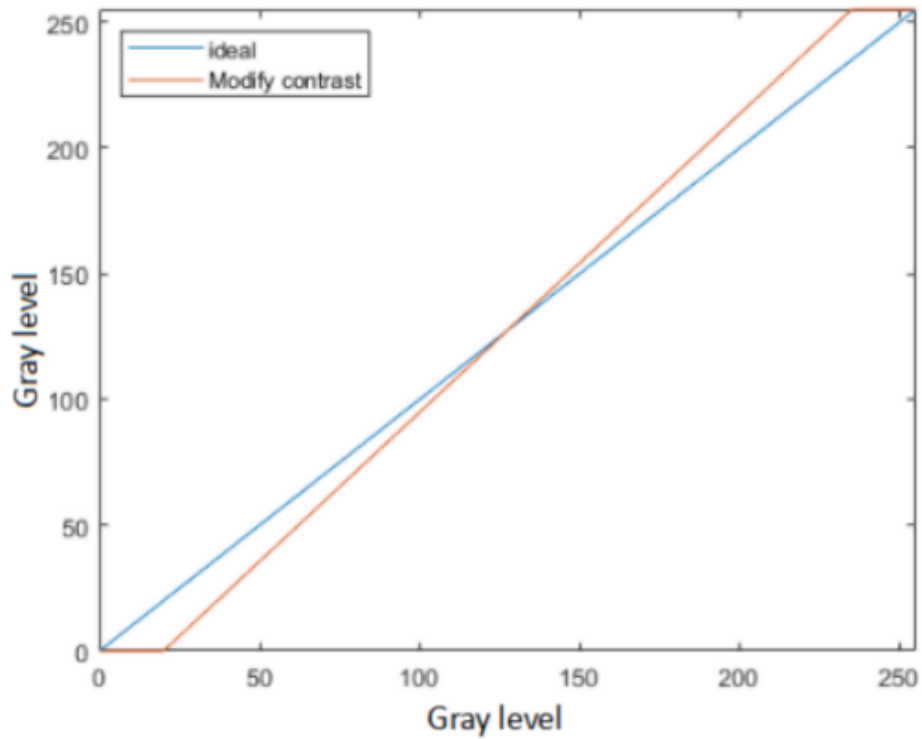


Figure 4.19: (1)Ideal situation with $C = 1$ (2)As discussed in Fig.4.13, the relationship between input gray and output gray is changed by increasing the contrast, thus increasing the number of pixels that will appear black or white on the SLM

Through bowman grating, we can know that the optimal contrast of SLM used in this experiment is 1.1. Therefore, after modifying the hologram sent to SLM, the relationship between its input gray level and output gray level is shown in Fig. 4.19.

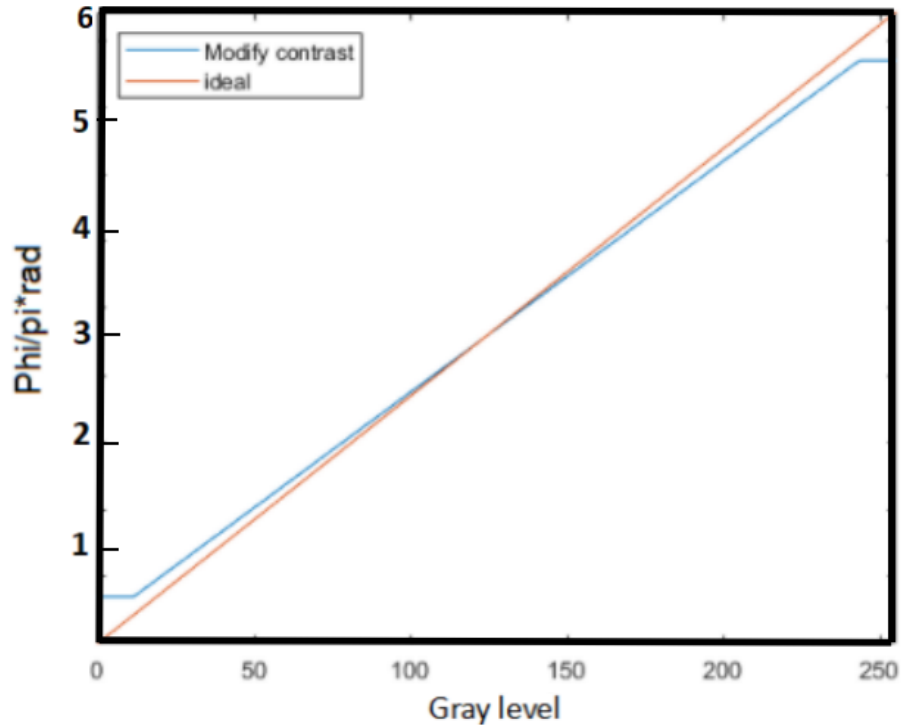


Figure 4.20: By adjusting the contrast, the original phase modulation curve was closer to the ideal 6π phase modulation curve

As shown in Fig. 4.20, Through the adjusted phase modulation curve, we can see that after adjustment, the SLM phase modulation can be as close as possible to the ideal situation, and close to the phase modulation of 6π .

Therefore, combining two methods of binary grating and Bowman grating, this chapter first obtains the actual phase modulation curve of SLM using binary grating, and compares it with the perfect phase modulation curve, and then obtains the best contrast through Bowman grating, so as to realize the calibration of SLM and make the phase modulation curve of SLM close to perfect as far as possible.

Chapter 5

Application of SLM in vortex beam ptychography

In the first and second chapters, some basic concepts and theoretical basis of vortex beam and ptychography are introduced. In the third chapter, SLM, the key instrument to generate vortex beams, and the principle of recovery of real-space images are further outlined. Therefore, the vortex beam ptychography imaging system with SLM as the core device can be designed.

Because the current research of ptychography mainly focuses on using the common laser, X-ray and electron microscopes, there are none reports on the research of combining vortex beam and ptychography. Considering that both Ptychography and vortices are widely used in the field of imaging, it is of great significance to apply vortices to Ptychography. This chapter first introduce the designs of the experimental device, and then demonstrates the actual imaging of the sample in the case of vortex beam as the probe, and determines the factors affecting the imaging effect.

5.1 Experimental set-up and data collection

5.1.1 Design principle of imaging system

As shown in Fig. 5.1, the principle of Ptychography is to scan a sample using a probe until the entire region of interest on the sample is scanned. Probes usually require a high degree of coherence, such as X-rays, monochromatic coherent light, etc. Under normal circumstances, in the scanning process, the sample area of two adjacent scans must be repeatedly illuminated to receive the far-field diffracted light field of the overlapping area information obtained by the probe scanning on the CCD. Fig. 5.2 shows the overlapping of a light probe with a width of E at a scanning step of G .

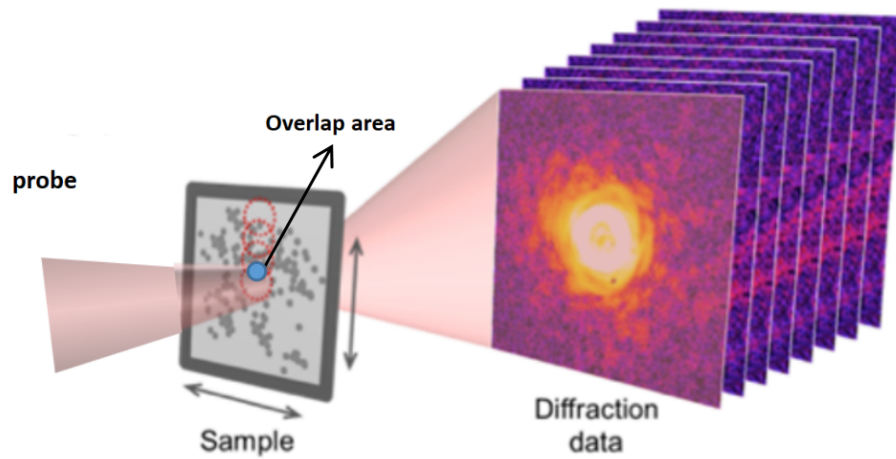


Figure 5.1: A diagram of a probe scanning a sample during ptychography. Figure courtesy of [7]

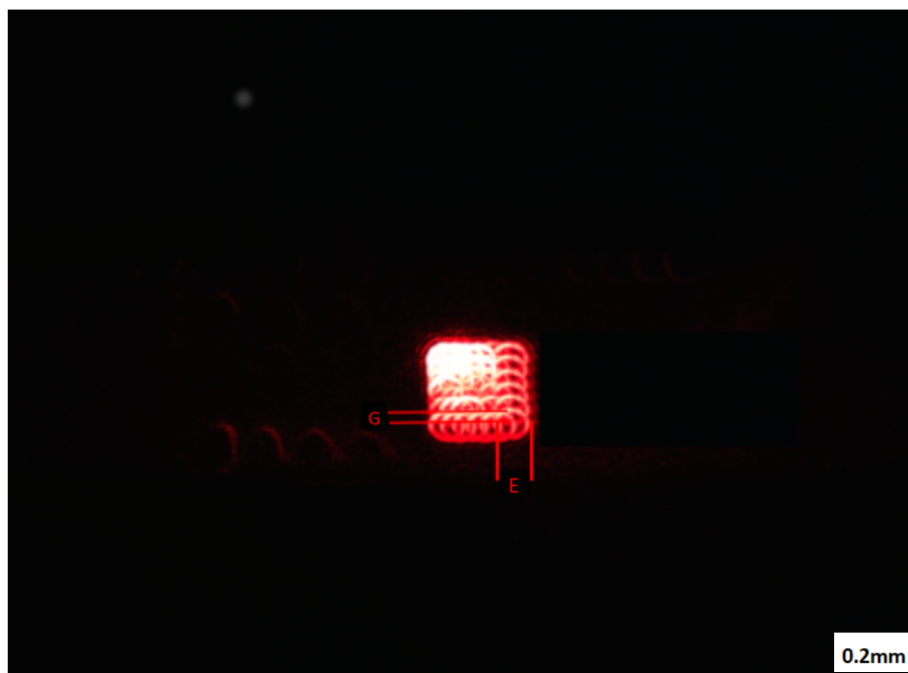


Figure 5.2: Overlapping scanning of a light probe on the sample surface. G is scanning step and E is probe width.

5.1.2 Design scheme of imaging system

According to the experimental requirements, the experimental platform shown in Fig. 5.3 was built. The laser with a wavelength of 632.8 nm realized a 4.5-fold beam expansion through lens 1 with a focal length of 20 mm and lens 2 with a focal length of 90 mm, adjusted the beam polarization by rotating the laser tube and polarizer 1 to ensure that the polarized beam is along the vertical direction, which is the original direction of LC molecules. After the slit filter filters out the unnecessary diffracted light, the beam passes through L4 and L5 and then converges to receive the diffraction pattern on the CCD.

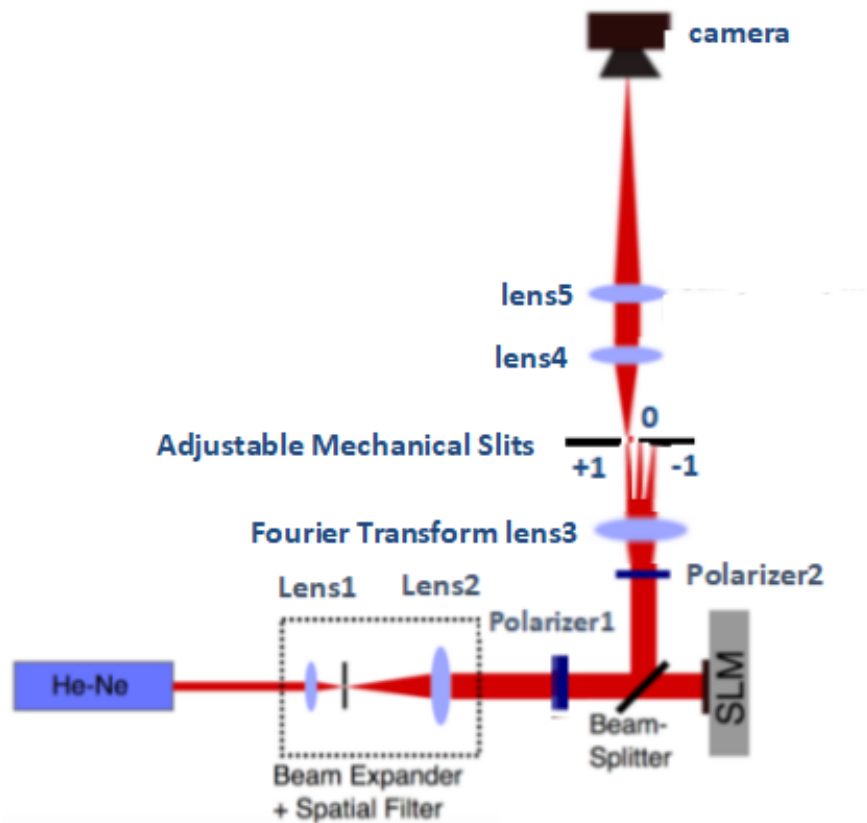


Figure 5.3: The optical set-up for imaging the scanning probe. The slit is used to block the unwanted diffracting beams.

Through the above design, an optical ptychography system is built, which can generate vortex beam and realize beam scanning at the same time. The main experimental unit picture is shown in the Fig. 5.4. After expanding

and collimating, the laser generates vortex or ordinary beams through SLM. Through adjusting the hologram patterns, the beam profile and positions can be turned. After the unwanted diffraction beams are blocked by a slit, the beam we want can be controlled to reach the CCD, so as to realize the purpose of scanning different parts of the sample.

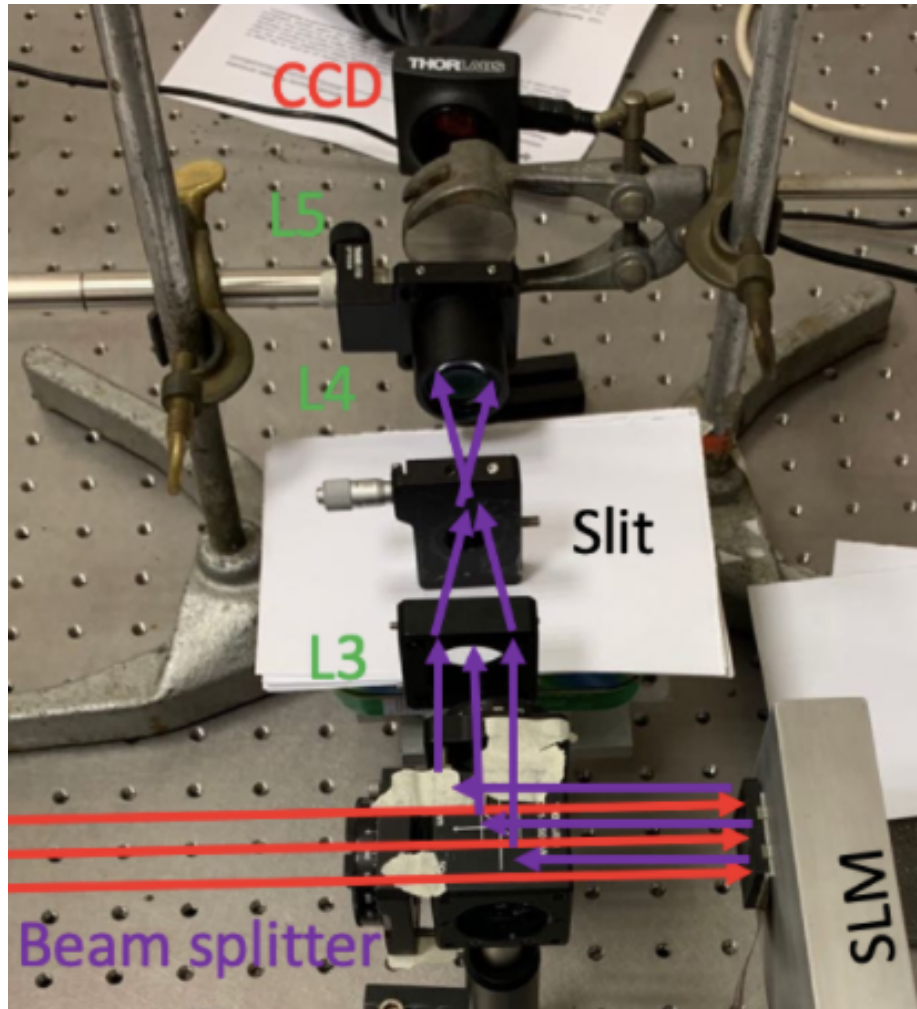


Figure 5.4: Optical set-up for the ptychography experiment. L4 and L5 are adjusted to either image the probe or the diffraction pattern of the probe.

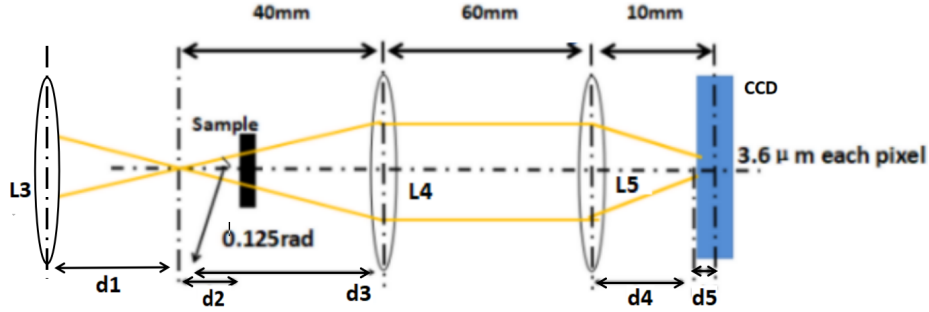


Figure 5.5: The optical set-up for ptychography with the sample placed in a defocused position with respect to the focal plane of the probe. Where d_1 is the focal length of L3, d_2 is the distance from the focus of L3 to the sample, d_3 is the distance from the probe focus to L4, d_4 is the distance from L5 to CCD camera, and d_5 is the distance from CCD camera plane to focal point of L5.

By changing the pixel width of grating element, we can control the beam deflection, so as to realize the purpose of scanning on the sample. Follow the Eqn.3.8, the scanning step can be calculated:

$$l_{step} = d_1 * \tan\theta = d_1 * \frac{\lambda}{LP} \quad (5.1)$$

In fact, due to the small scanning area of the probe, it is difficult to use the physical measurement on the existing equipment. Therefore, the similar triangle rule is used in this experiment to calculate the size of the probe on the sample plane according to the size of the probe on the CCD. By measuring the parameters (SLM pixel size, focal lens, pixel width of the grating element) of the devices, we can calculate the probe size on the sample surface and obtain the schematic diagram as shown in the Fig. 5.5, When the sample is not placed, we can get the probe; when the sample is placed between slit and L4, we can get the diffraction pattern through the sample.

The calculation steps are as follows:

$$D_{probe} = \frac{G*(d_4+d_5)}{d_5} * d_2 = \frac{nw*(d_4+d_5)}{d_5} * d_2 \quad (5.2)$$

where D_{probe} is the diameter of Probe size on the sample surface, w is the pixel width of the CCD, n is the number of pixels of the probe diameter on the CCD.

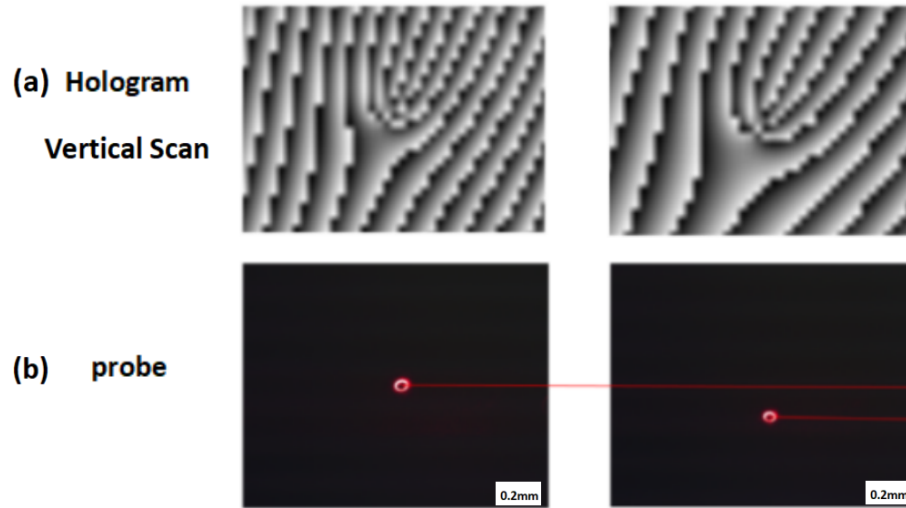
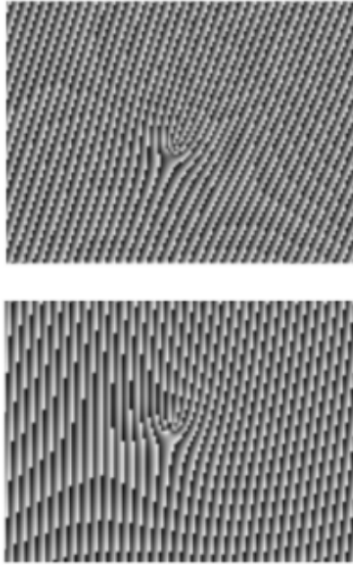


Figure 5.6: (a) is the grating to achieve vertical deflection required by the experiment. By combining the fork gratings and the blazed gratings, and by changing the pixel period of the gratings, a grating which can realize both vertical scanning and vortex light generation is obtained. (b) is the position of the probe corresponding to the two gratings. The red line clearly reflects the change of the position of the probe in the vertical direction (Vertical scanning).

(a) hologram:horizontal scan



(b) Probe



Figure 5.7: (a) is the grating to achieve horizontal deflection required by the experiment. By combining the fork gratings and the blazed gratings, and by changing the pixel period of the gratings, a grating which can realize both horizontal scanning and vortex light generation is obtained. (b) is the position of the probe corresponding to the two gratings. The red line clearly reflects the change of the position of the probe in the horizontal direction(Horizontal scanning).

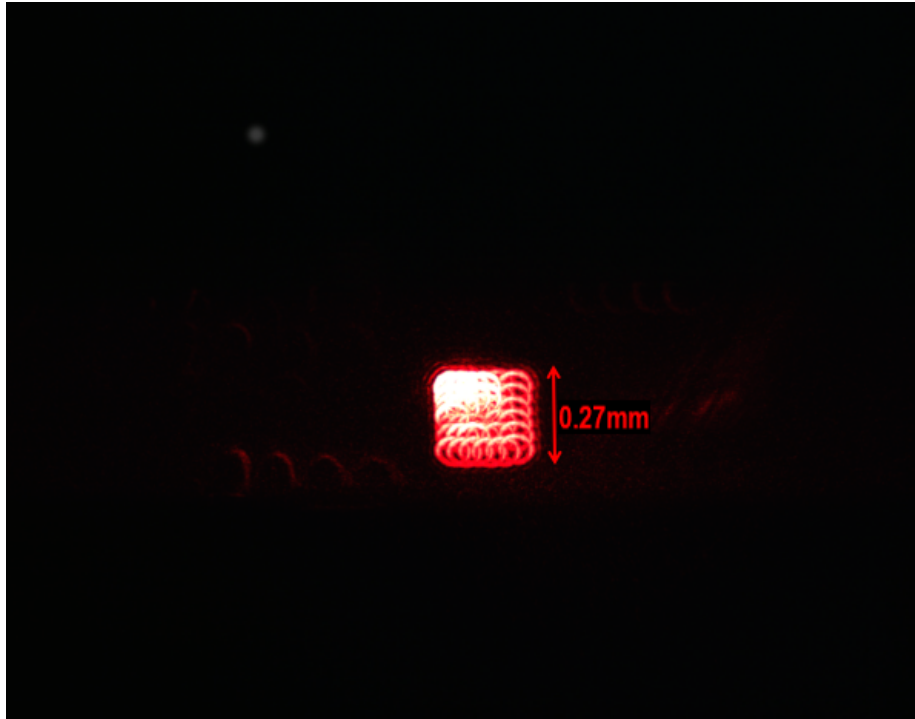


Figure 5.8: Probe scanning range calculated from data

5.1.3 Data collection

In this experiment, the thin transparent plastic sheet with a scratch structure on the surface is selected as the sample, and the thickness of the sample is 1.44 mm, as shown in Fig. 5.9. In order to explore the influence of probe on imaging effect, this experiment is Carried out from two aspects: the order of vortex beam and defocus.

First of all, the influence of vortex beam order on imaging effect is explored. Using 632.8 nm polarized light as incident beam source, after SLM modulation, the position of sample 7×7 is scanned. The diameter of each probe was measured to be 30 pixels. At the same time, by changing the pixel width of grating element, we could control the deflection angle of the probe and scan on the sample, and controlled the overlap ratio of the probe to be about 75%.

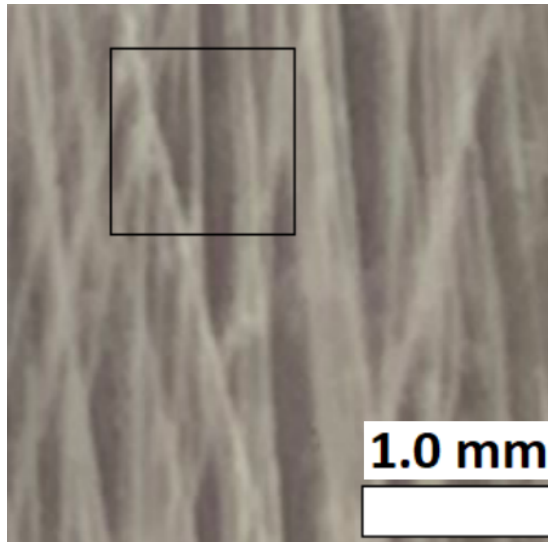


Figure 5.9: The image of the scratched area taking using mobile phone (Huawei, P30, camera apps). The scale bar is calculated using the information about the physical size of the sample and the pixel size of the sample in the image.)

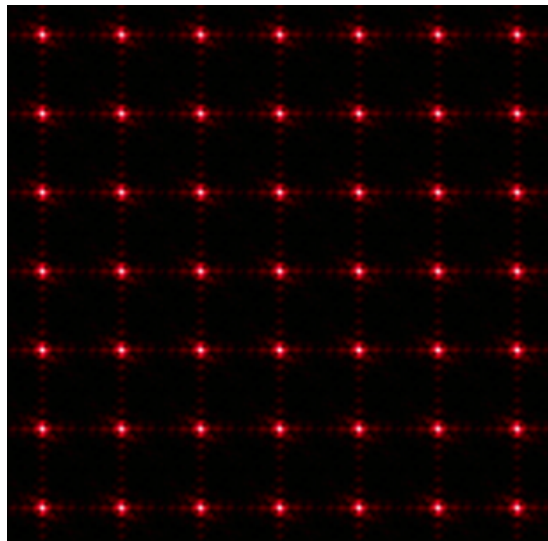


Figure 5.10: The montage of the diffraction pattern of a normal (non-vortex) beam (by setting $l=0$) as it scans the sample in 7x7 positions.

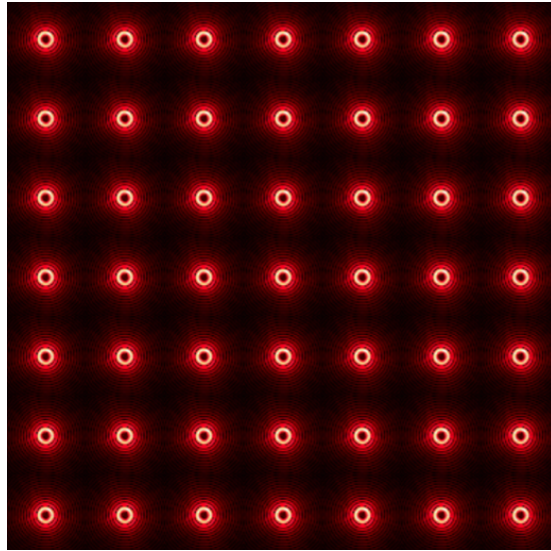


Figure 5.11: Diffraction of the sample by vortex beam of order 4.

Fig. 5.10 and Fig. 5.11 are the recorded images, which show the diffraction patterns of non vortex beam and vortex beam under the same defocus condition. In addition, the effects of different orders of vortex beam on image quality are also studied. The diffraction patterns of different orders of vortex beams after transmitting the sample at the same scanning position are shown in Fig.5.12, and Fig.5.13 shows the diffraction patterns under different defocus obtained by adjusting defocus with the vortex beam of $\ell = 5$ as an example.

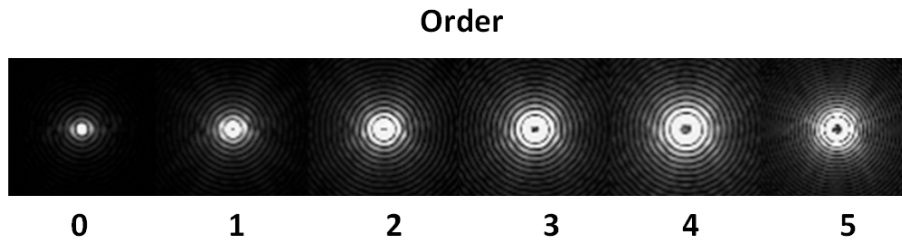


Figure 5.12: the diffraction patterns of different order vortex beam at the same position

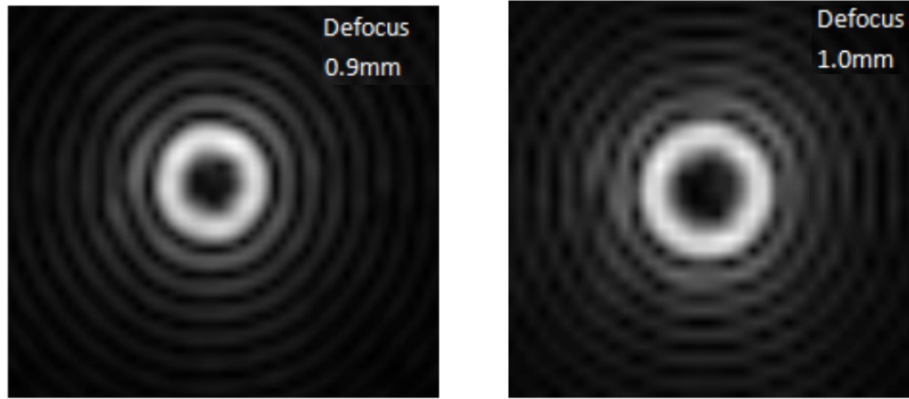


Figure 5.13: Diffraction pattern of vortex beam with different focus at the same position for $\ell = 5$.

5.2 Reconstruction and quantification of quality

In order to compare the recovery effects of vortex beam and non vortex beam on the same sample, 49 diffraction patterns were extracted and the ePIE algorithm was implemented by Matlab program. After convergence, the reconstructed image is shown in the Fig.5.14.

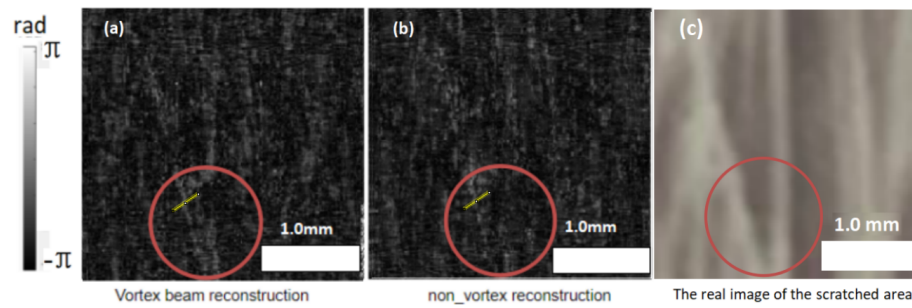


Figure 5.14: The phase reconstruction images of the samples were compared by using the vortex probe(a) and the non-vortex probe(b), the yellow line represents the sampling area of the line profile, (c) is the real image of the scratch structure in the same scale

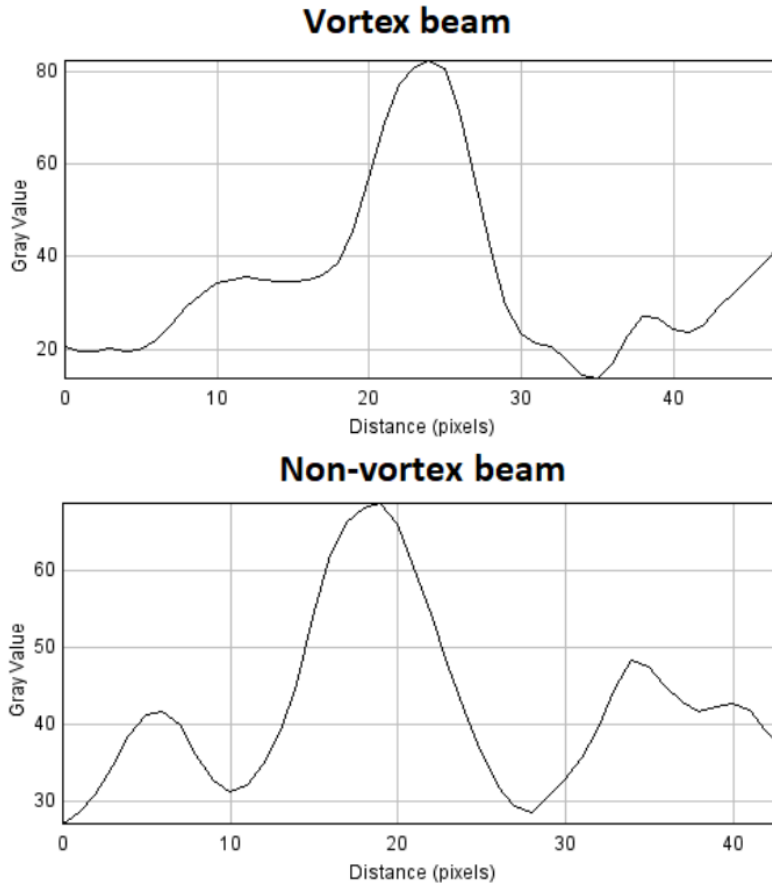


Figure 5.15: The sample is reconstructed by using vortex beam and non-vortex beam, extracting a line profile across a specific scratch feature to obtain the gray distribution of the specific line. The horizontal axis represents the length of the line, and the vertical axis reflects the gray values at different positions.

As shown in Fig. 5.14, extracting the line profile of a specific scratch feature from the reconstructed image of the vortex beam and the non-vortex beam, the grayscale distribution shown in Fig. 5.15 can be obtained. It can be clearly seen that when the vortex beam is used when reconstructing the sample, the gray value of the scratched structure is more obvious, and at the same time, the noise signal is relatively weak in the non-scratched area, which can prove that the image reconstructed by vortex beam has a higher contrast. In order to further study the ptychography, the vortex beam is used as the probe light source to reconstruct the amplitude and phase of the sample. In addition, in order to compare image quality, we use peak signal-to-noise ratio(PSNR) to

compare, the PSNR value is calculated as follows [90]:

$$PSNR = 10 \times \log_{10} \frac{(2^a - 1)}{MSE} \quad (5.3)$$

Among them, a is the number of bits of each sampled value, MSE is the mean square error between the original image and the processed image, and the calculation process is shown in Eqn. 3.16. PSNR is the most common and widely used objective measurement method to evaluate image quality. However, many experimental results show that the score of PSNR is not completely consistent with the visual quality of human eyes. It is possible that the higher PSNR looks worse than the lower PSNR. This is because the sensitivity of human vision to error is not absolute, and its perception result will be affected by many factors (for example, human eyes are more sensitive to contrast difference with lower spatial frequency, higher sensitivity to brightness contrast difference and higher sensitivity to chroma, and the perception result of human eyes to an area will be affected by its surrounding areas) [91].

Through the equation we talked above, PSNR values of the recovered sample and the original sample can be calculated, and the data as shown in Tbl. 5.1. It can be clearly seen that both amplitude and phase images have a high recovery quality when the sample is reconstructed by combining vortex beam and ptychography, and the image shows higher quality when the sample phase is restored. Since the probe function is updated iteratively when ePIE algorithm is used, the phase and amplitude of the probe function can be recovered at the end of reconstruction as well. The amplitude and phase images of the probe are shown in Fig.5.17.

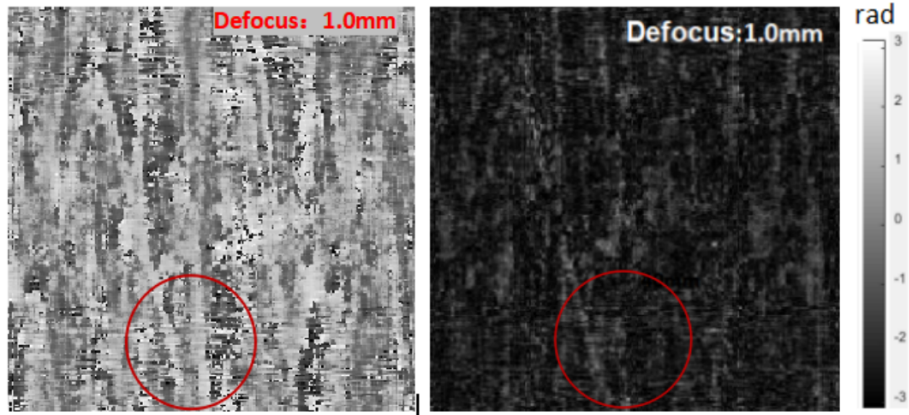


Figure 5.16: The amplitudes(left) and phases(right) of the sample when reconstruction is carried out.

	Amplitude	Phase
PSNR	62.3	71.3

Table 5.1: PSNR values of amplitude and phase reconstructed images



Figure 5.17: The amplitudes(left) and phases(right) of the estimate of the probe after the reconstruction.

The previous experiments verify the feasibility of applying vortex beams in an ptychography experiment, and then change the defocus by changing the distance from the sample to slit position (which defines the plane where the diffraction pattern is focused), and keep the topological charge of the vortex beam same, so as to study the influence of different defocus on the quality of sample reconstruction. Through the experimental data and reconstruction of the sample, we can find that the reconstruction quality of the sample also changes with the change of defocus. By comparing the PSNR value and grayscale distribution of line profile, it can be found that when the defocus is 1.0mm, the reconstructed image has the clearest scratch structure and less noise, and the reconstruction effect is the best. Fig. 5.18 shows the reconstructed result. Fig. 5.19 shows the grayscale distribution of line profile, Tbl. 5.2 shows the PSNR values recovered under different defocus.

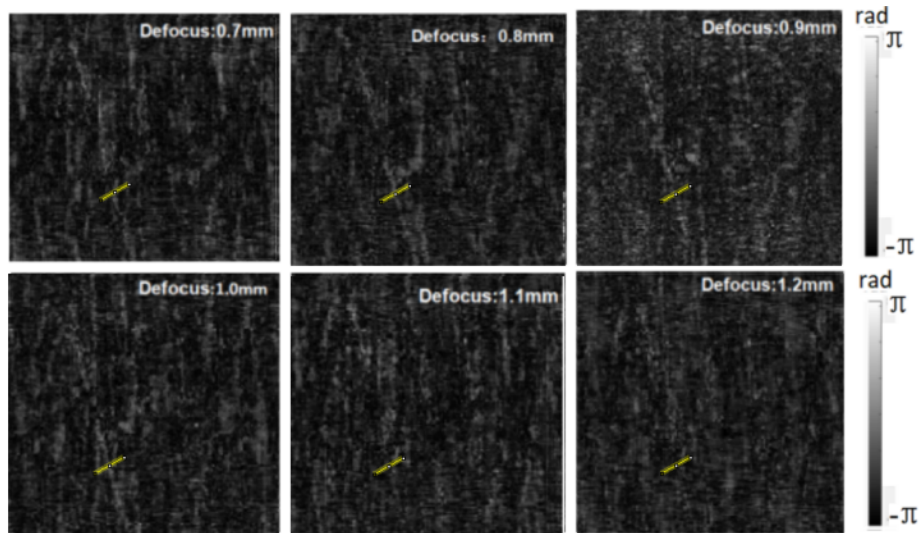


Figure 5.18: The comparison of the phase reconstructed images of the sample, for different defocus condition, the yellow line represents the sampling area of the line profile.

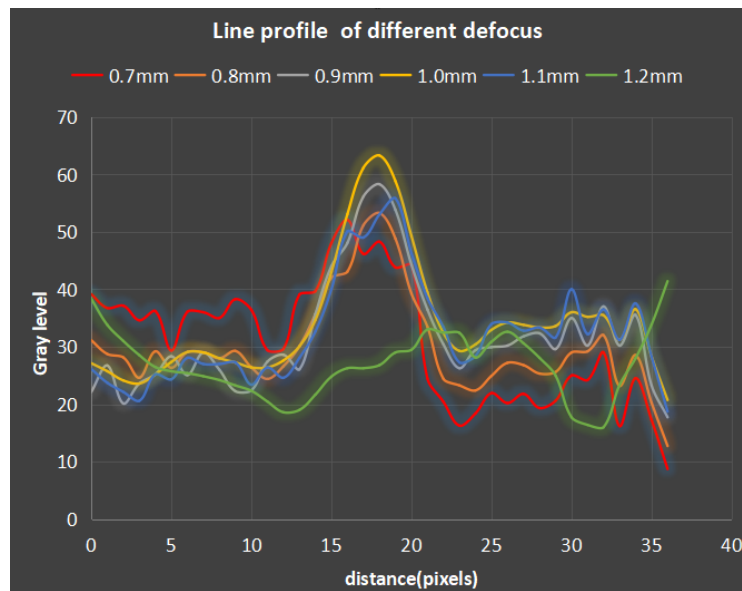


Figure 5.19: Line profiles are drawn across specific scratch characteristics under different defocus conditions. The horizontal axis represents the length of the line, and the vertical axis reflects the gray values at different positions.

Defocus	0.7mm	0.8mm	0.9mm	1.0mm	1.1mm	1.2mm
PSNR	56.5	58.6	60.5	62.4	56.1	54.6

Table 5.2: PSNR values of phase reconstructed images under different defocus. It can be seen from the PSNR value that when the Defocus value is 1.0mm, the PSNR value is the highest and the image quality is the best

In order to further study the influence of the vortex beam order on the reconstruction quality of the sample, the vortex beam order is changed under the condition that defocus is unchanged, and the diffraction patterns of different orders of vortex light are reconstructed. The reconstructed image of the sample is shown in Fig. 5.20, the amplitude and phase reconstruction images of the probe are shown in Fig. 5.21, and the PSNR value of the reconstructed image of the sample is shown in Tbl. 5.3.

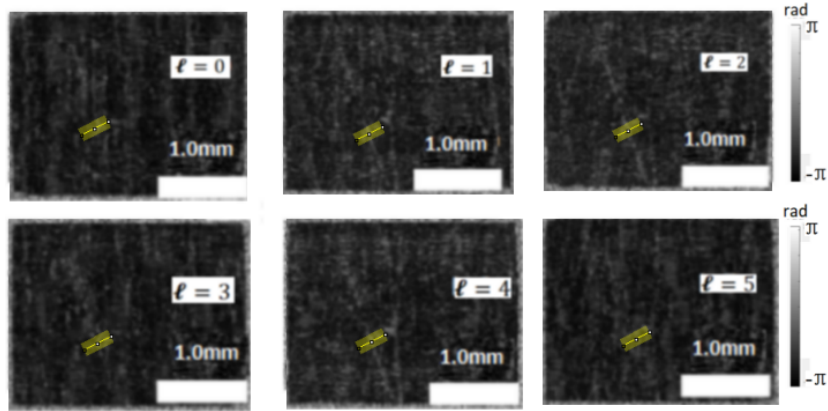


Figure 5.20: Sample Phase reconstruction of different ℓ vortex beam (Defouse=1.0mm), the yellow line represents the sampling area of the line profile.

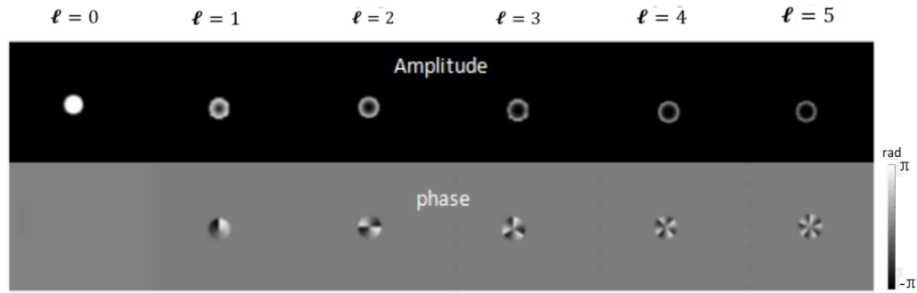


Figure 5.21: The amplitudes(top) and phases(bottom) of the probe when reconstruction is completed, for different ℓ



Figure 5.22: Line profiles are drawn across specific scratch characteristics under different order conditions. The horizontal axis represents the length of the line, and the vertical axis reflects the gray values at different positions.

Order	0	1	2	3	4	5
PSNR(Phase)	56.5	58.4	60.5	61.2	62.4	58.3

Table 5.3: PSNR values of phase reconstructed images for different order. It can be seen from the PSNR value that when the Order value is 4, the PSNR value is the highest and the image quality is the best

5.3 Effect of defocus, effect of topological charge of the vortex beams

The content of this chapter mainly describes how the topological charge order of vortex beam and defocusing affect the reconstruction quality when the sample is reconstructed by the combination of the vortex beam and the non vortex beam with ptychography, and makes theoretical analysis on it. According to the previous experiments, as shown in Fig.5.12, under the appropriate diffraction distance, the spatial light modulator can load the phase fork gratings with different topological charges by setting the value of ℓ to generate different vortex beams. By comparing the vortices and non-vortices in Fig. 5.10 and Fig. 5.11, It is found that when the vortex beam is used as the illumination source, the energy of the vortex beam is mainly concentrated in the ring because the central light intensity of the vortex beam is 0. Therefore, compared with the ordinary non-vortex beam, the effective utilization rate of the illumination source is improved when scanning the sample. In addition, the quasi non-diffractive property of vortex beam can reduce the stray light generated in the transmission of the illumination source [92], reduce the noise to a certain extent, and enhance the contrast of imaging.

According to the experimental image shown in Fig.5.12, when the topological charge increases, the vortex spot will also increase, but the diffraction halo tends to increase first and then decrease. From the reconstructed image shown in Fig. 5.20, it can be seen that when the diffraction halo changes with the order of vortex light, the recovery quality will also change. As shown in Fig. 5.22, when using different order of vortex beam as probes, the specific scratch structure of the reconstructed image of the sample is analyzed. It can be seen that the contrast of the reconstructed image is affected by the order of vortex beam, and when $\ell = 4$, the scratch signal is the clearest and the noise is less. At the same time, the PSNR value of the reconstructed image in Tbl. 5.3 reflects that the reconstructed image is the clearest when $\ell = 4$. Therefore, when using different order of vortex beam to reconstruct images, with the increase of diffraction halo, if the scanning steps are the same, the overlap rate will increase accordingly, so that more details can be displayed in the reconstructed image and the reconstruction quality is higher.

Through the research of defocus on the quality of reconstructed image, we find that defocus is also a major factor affecting image quality. As shown in Fig. 5.18, through the study of the specific scratch structure, the grayscale distribution shown in Fig. 5.19 and the PSNR value of the reconstructed image shown Tbl. 5.2 are obtained by analysis. Through comparison, it is found that the amount of defocus will affect the contrast and resolution of the reconstructed image when the same order of vortex light is used as the probe. This is mainly manifested in the case of 1mm defocus, large gray value of scratch structure, small noise signal, highest PSNR, and highest reflection imaging quality. Due to the complicated influence of defocusing on image quality, there is no systematic research yet. But we can find that if the defocus is larger, it means that a larger

sample can be sampled at the same position. If the defocusing amount is very small, the overlap ratio will decrease when the same translation step is used, which will affect the reconstruction quality. To obtain the same overlap rate, it is necessary to reduce each translation step of the probe. If it is necessary to complete the sampling of the same region, it takes a longer time to obtain more diffraction images. Therefore, it is necessary to choose the appropriate defocusing amount and scanning step length when imaging the sample.

Chapter 6

Conclusion and future work

In recent years, lensless coherent diffraction imaging technology has been widely studied because of its simple system structure, low manufacturing cost, and not limited by the numerical aperture and relative aperture of lens, which is helpful to improve the resolution. With the increasing enrichment and improvement of phase retrieval algorithm, the development of laminated imaging theory is becoming more and more perfect. In this paper, based on the theory of stack imaging and phase retrieval algorithm, some parameters which affect the reconstruction quality of stacked imaging are studied. In this paper, the theoretical basis of stacked imaging is briefly summarized, and then the three key parameters that affect the imaging performance of the stacked imaging system are studied, focusing on the probe type, vortex optical topological charge and defocusing amount. The following is a summary of the main work completed in this thesis and the future work is prospected.

6.1 The main work and research results

(1) In this thesis, a ptychography system based on vortex beam is designed. Using spatial light modulator as the core equipment, we can have more freedom to adjust the probe, the overlap rate between probes and the distribution of overlapping area between probes, which makes the shape, size and scanning mode of the probe no longer subject to strict restrictions, making the ptychography more feasible, and the optical experimental operation of the ptychography system is more simple, and can also get better imaging quality. (2) The effect of the parameters of the vortex beam on the reconstructed image quality is verified by optical experiments, and the systematic analysis is made.

6.2 Future research directions

Since ptychography is a lens-less coherent diffraction technique, the complex amplitude information of the object can be recovered without the limitation of

sample size. Due to its high quality and fast processing speed, it has been widely used in the fields of microscopic imaging, wide-field imaging and information security, etc. However, there are still some problems to be further improved. (1) The current work is to directly image transparent or translucent objects, while some opaque objects cannot be processed. The next step is to study reflection lamination imaging, which is not limited to the processing of transparent objects. In this way, ptychography can also be applied to the measurement of object surface shape and other fields, making ptychography more practical. (2) Ptychography is now used only to process static samples, but it is useless for recording and measuring dynamic objects. Next, real-time dynamic tracking measurement technology can be combined with ptychography to further expand the application scope of ptychography.

Appendix A

Mathematical derivation of diffraction pattern of a binary phase grating

From the structure of the binary phase grating element defined in Fig. 4.2, we know that the phase delay of the left part of the grating element is $\Delta\varphi$, and the phase delay of the right part is 0. The phase function for the grating element, t_e can be written as a convolution integral, as follows:

$$t_e(x, y) = \exp(i\Delta\psi) \times \text{rect}\left[\frac{x + L/4}{L/2}\right] + 1 \times \text{rect}\left[\frac{x - L/4}{L/2}\right] \quad (\text{A.1})$$

So the phase function for the grating as a whole, t_g , should look like this:

$$t_g(x, y) = t_e(x', y) \otimes \sum_{n=1}^N \delta(x' - x_n) = \int_{-\infty}^{+\infty} t_e(x', y) \sum_{n=1}^N \delta(x' - x_n) dx' \quad (\text{A.2})$$

where N is the number of the grating element in the grating, x_n is the central coordinate of n^{th} element and the value is nL , where L is the length of the grating element. The intensity distribution behind the lens should be the Fourier transform of Eqn.A.2. According to the convolution theorem [93], the Fourier transform of the convolution integral can be written as a product of their corresponding Fourier transform:

$$\mathcal{F}(t_g) = \mathcal{F}(t_e) \times \sum_{n=1}^N \mathcal{F}(\delta(x' - x_n)) = T_e \sum_{n=1}^N T_n \quad (\text{A.3})$$

where T_e is the Fourier transform of the phase function for the grating element t_e :

$$T_e = \mathcal{F}(t_e) \quad (\text{A.4})$$

and T_n is the Fourier transform of the n^{th} delta function:

$$T_n = \mathcal{F}(\delta(x - x_n)) \quad (\text{A.5})$$

Follows the principle of Fourier transform calculation [94], the calculation process is as follows

$$\begin{aligned} T_e &= \int_{-\infty}^{+\infty} t_u e^{ikx} dx \\ &= \int_{-L/2}^0 e^{i\Delta\phi} e^{ikx} dx + \int_0^{L/2} 1 e^{ikx} dx \end{aligned} \quad (\text{A.6})$$

Replacing $e^{i\Delta\phi}$ with a and 1 with b makes the calculation easier.

$$\begin{aligned} T_e &= 1/ik(a - ae^{-ikL/2} + be^{ikL/2} - b) \\ &= 1/ik[(ae^{-ikL/4})(e^{ikL/4} - e^{-ikL/4}) + be^{ikL/4}(e^{ikL/4} - e^{-ikL/4})] \\ &= 1/ik(2isinc(kL/4))[ae^{-ikL/4} + be^{ikL/4}] \\ &= L/2sinc(kL/4)(ae^{-ikL/4} + be^{ikL/4}) \end{aligned} \quad (\text{A.7})$$

$$\sum_{n=1}^N T_n = \int_{-\infty}^{+\infty} \sum_{n=1}^N \delta(x - x_n) e^{ikx} dx \quad (\text{A.8})$$

$$\begin{aligned} \sum_{n=1}^N T_n &= \sum_{n=1}^N e^{ikx_n} = \sum_{n=1}^N e^{iknL} = \frac{e^{ikL} - e^{ikL(N+1)}}{1 - e^{ikL}} \\ &= \frac{e^{ikL}(1 - e^{iNkL})}{1 - e^{ikL}} = e^{\frac{i(N+1)kL}{2}} \frac{\sin NkL}{\sin kL} \end{aligned} \quad (\text{A.9})$$

It can be concluded from the above calculation:

$$\mathcal{F}(t_g) = \frac{1}{2} \text{sinc}\left(\frac{kL}{4}\right) (ae^{-\frac{ikL}{4}} + be^{\frac{ikL}{4}}) e^{\frac{i(N+1)kL}{2}} \frac{\sin NkL}{\sin kL} \quad (\text{A.10})$$

Thus, the diffraction pattern formula of whole grating can be concluded from the above calculation:

$$I = |\mathcal{F}(t_g)|^2 \propto \left| (ae^{-\frac{ikL}{4}} + be^{\frac{ikL}{4}})^2 \right| \quad (\text{A.11})$$

Where I is the intensity of each beam spot.

For the intensity of 0-order beam spot, I_0 , the value of k is 0 and then apply k to EQN.A.11:

$$I_0 \propto |(a+b)^2| \propto |(e^{i\Delta\phi} + 1)^2| = \left(\cos\frac{\Delta\phi}{2}\right)^2 = \frac{1 + \cos\Delta\phi}{2} \quad (\text{A.12})$$

where we have resubstituted $a = e^{i\Delta\phi}$ and $b = 1$. Therefore, the calculation between zero-order beam spot intensity and grating gray scale can be obtained.

Appendix B

Mathematical derivation of diffraction pattern of a Bowman phase grating

From the structure of the bowman phase grating element defined in Fig.4.11, the phase function for the gating element t_u can be written as below

$$t_u(x, y) = \begin{cases} e^{i\phi_{min}} & -L/2 \leq x \leq -\frac{L}{2C} \\ e^{i(C\frac{\Delta\phi}{L}x + \frac{\phi_{min} + \phi_{max}}{2})} & -\frac{L}{2C} < x < \frac{L}{2C} \\ e^{i\phi_{max}} & \frac{L}{2C} \leq x \leq L/2 \end{cases} \quad (B.1)$$

Where ϕ_{min} is the minimal phase delay which corresponding to the 0-grey value, ϕ_{max} is the maximum phase delay which corresponding to the 0-grey value, C is the contrast, and the slope of the relationship between the phase delay and the x value can be controlled, L is the length of grating element. So the phase function for the grating as a whole, t_g , should look like this

$$t_g(x, y) = t_u(x', y) \otimes \sum_{n=1}^N \delta(x' - x_n) = \int_{-\infty}^{+\infty} t_u(x', y) \sum_{n=1}^N \delta(x' - x_n) dx' \quad (B.2)$$

where N is the number of the grating element in the grating, x_n is the central coordinate of n^{th} element and the value is nL , where L is the length of the grating element. The intensity distribution behind the lens should be the Fourier transform of Eqn.B.2. According to the convolution theorem [93], the Fourier transform of the convolution integral can be written as a product of their corresponding Fourier transform:

$$\mathcal{F}(t_g) = \mathcal{F}(t_e) \times \sum_{n=1}^N \mathcal{F}(\delta(x' - x_n)) = T_u \sum_{n=1}^N T_n \quad (B.3)$$

where T_u is the Fourier transform of the phase function for the grating element t_u :

$$T_u = \mathcal{F}(t_u) \quad (\text{B.4})$$

and T_n is the Fourier transform of the n^{th} delta function:

$$T_n = \mathcal{F}(\delta(x - x_n)) \quad (\text{B.5})$$

Follows the principle of Fourier transform calculation [94], the calculation process is as follows:

$$T_u = \frac{2\sin(\frac{k\pi}{C})}{C + k} \quad (\text{B.6})$$

Where the value of k is $\frac{2\pi n}{\lambda}$

$$\sum_{n=1}^N T_n = \int_{-\infty}^{+\infty} \sum_{n=1}^N \delta(x - x_n) e^{ikx} dx \quad (\text{B.7})$$

$$\begin{aligned} \sum_{n=1}^N T_n &= \sum_{n=1}^N e^{ikx_n} = \sum_{n=1}^N e^{iknL} = \frac{e^{ikL} - e^{ikL(N+1)}}{1 - e^{ikL}} \\ &= \frac{e^{ikL}(1 - e^{iNkL})}{1 - e^{ikL}} = e^{\frac{i(N+1)kL}{2}} \frac{\sin NkL}{\sin kL} \end{aligned} \quad (\text{B.8})$$

It can be concluded from the above calculation:

$$\mathcal{F}(t_g) = T_u \sum_{n=1}^N T_n = \frac{2\sin(\frac{k\pi}{C})}{C + k} e^{\frac{i(N+1)kL}{2}} \frac{\sin NkL}{\sin kL} \quad (\text{B.9})$$

Thus, the diffraction pattern formula of whole grating can be concluded from the above calculation:

Appendix C

Matlab code to generate CGH and receive diffraction pattern

```
clear all;
close all;
s=2; % # of pixels per fringe.
c=18
Secondaryscreen = false; % True place figure on secondary
    screen.
imageName='SLMpat'; % This is the name of the file
    that has the pattern
ImageName='SLMimg'
Nx = 1920; % # of pixels in x-dimension of
    Cambridge SLM
Ny = 1080; % # of pixels in y-dimension of
    Cambridge SLM
R_mask=200;
ell=5; % This is the value of the topological charge
    of the LG beam
[X, Y] = meshgrid(-Nx/2+1:Nx/2, -Ny/2+1:Ny/2);
max_phase_shift=2*pi;
r1 = zeros(Ny,Nx); % used to declare the
    matrix and its dimension
cols = 0:Ny-1; % create a variable for numbering the
    columns
r=conj(cols')
%r1(:, find(mod(cols, s*2)<s))=2*pi;
r1=mod(r, c)/c
```

```

        r6= repmat(r1,1,1920)
        mask=((sqrt(X.^2+Y.^2))<R_mask);
R = sqrt(X.^2 + Y.^2); % Radial distance
phi = atan2(Y, X); % Azimuthal angle
phi1 = ell*phi + 1/s*X; % Phase of each pixel;
r2=mod(phi1,2*pi)/(2*pi); % Phase mod 2 pi in units
    of 2pi;
r3=mod(phi1+r1*2*pi,2*pi)/(2*pi)/(2*pi); % compound
    Phase mod 2 pi in units of 2pi;
r4=r3.*mask;
clims = [0 1];
if Secondaryscreen
    Left=1920; % Pixelwidth of main screen
    Bot=0; % Main screen height - SLM height in pixels
    position = [Left Bot Nx Ny];
    figure('Position',position,'MenuBar','none');
    axes('Position',[0 0 1 1]);
else
    figure();
    end
    imshow(r4,clims);
%colormap(gray);
axis equal;
axis off;
fileType = 'bmp';
sell=num2str(ell);
s2s=num2str(s);
imfname=[imName,'s',s2s,'l',sell,'.bmp'];
imwrite(r4, imfname, fileType);
pathName='C:\Program Files\Thorlabs\Scientific Imaging\
    DCx_Camera_Support\Develop\DotNet';

exposureTime = 0.050;

addpath(pathName);
NET.addAssembly([pathName,'\uc480DotNet.dll']);
% Create camera object handle
cam = uc480.Camera;
% Open the 1st available camera
cam.Init(0);
% Set display mode to bitmap (DiB)
cam.Display.Mode.Set(uc480.Defines.DisplayMode.DiB);
% Set color mode to 8-bit RGB
cam.PixelFormat.Set(uc480.Defines.ColorMode.RGBA8Packed);
% Set trigger mode to software (single image acquisition)
cam.Trigger.Set(uc480.Defines.TriggerMode.Software);

```

```

% Allocate image memory
[~, MemId] = cam.Memory.Allocate(true);

% Setting Gain
% cam.Gain.Hardware.Boost.GetSupported()
% uc480.GainBoost.SetEnable(0)
% Camera.Gain.Hardware.Boost( )
[~, rrr]=cam.Gain.Hardware.Factor.GetRed();
[~, rrr]=cam.Gain.Hardware.Factor.GetDefaultRed();
cam.Gain.Hardware.Factor.SetRed( int32(0) );
cam.Gain.Hardware.Factor.SetBlue( int32(0) );
cam.Gain.Hardware.Factor.SetGreen( int32(0) );

cam.Timing.Exposure.Set(exposureTime);
cam.Timing.Exposure.Get();
% Obtain image information
[~, Width, Height, Bits, ~] = cam.Memory.Inquire(MemId);
cam.Acquisition.Freeze(uc480.Defines.DeviceParameter.Wait
);

% Copy image from memory
[~, tmp] = cam.Memory.CopyToArray(MemId);
% Reshape image
Data = reshape(uint8(tmp), [Bits/8, Width, Height]);
Data = Data(1:3, 1:Width, 1:Height);
Data = permute(Data, [3,2,1]);
Data=uint8(Data);
figure; imshow(Data, []);
cam.Exit;
fileType = 'bmp';
sell=num2str(s);
s2s=num2str(c);
imfname=['D:\New_Folder ', ImageName, 's', s2s, 'l', sell, '.bmp
'];
imwrite(Data, imfname, fileType);

```

Appendix D

Matlab code for ePIE algorithm function

```
function [rdiffpats , ddiffpats ,probeOrig , positions] =ePIE  
    (big_obj, sizeObj, sizeCCD, side, ratio)
```

```
%%% Ptychography (optical)  
% 1. initiate probe positions  
% 2. create complex probes  
% 3. couple each probe to diff patt of model image  
%  
% INPUTS  
% big_obj      big extended object  
% sizeObj      size of extended object  
% sizeCCD      size of CCD / probe / each position's exit  
%              wave  
% side         1D scan size  
% ratio        ratio of probe size to CCD array size  
%  
% OUTPUTS  
% rdiffpats    real space exit wave  
% ddiffpats    propagated exit wave (i.e. FFT'ed)  
% oROI         origion of region of interest  
% probe_orig   probe  
% positions    scan positions
```

```
rng(2, 'twister')
```

```
show_image = 0;  
beam_stop = 0;
```

```

finite_CCD = 0;
finiteratio = 0;
diffpattnoise = 0;

% make probe positions (pixel size and real resolution
% need to be specified!)
positions = Grid_Scan(sizeObj, sizeCCD, side);
[Xmin, Ymin, Xmax, Ymax] = Find_Scan_Area(positions,
sizeCCD);

numApertures = max(size(positions));

X = positions(:,1);
Y = positions(:,2);

figure(2)
    scatter(positions(:,1), positions(:,2), 'bo'); grid
        on; grid minor; axis square; % check to see grid
        points
    xlim([0 sizeObj(2)])
    ylim([0 sizeObj(1)])
    title('Pixel_scan_positions')
    xlabel('Position_(px)')
    ylabel('Position_(px)')

%% make complex probe using positions
probeOrig = single(Make_Circle_Mask(round(ratio*sizeCCD
(1)),sizeCCD(1)));

%% make individual probe data (apply finite CCD and beam
% stop effect )
diffpats = zeros(sizeCCD(1), sizeCCD(2), numApertures, '
single');
rdiffpats = zeros(sizeCCD(1), sizeCCD(2), numApertures, '
single');
diffpats_og = zeros(sizeCCD(1), sizeCCD(2), numApertures,
'single'); % used as buffer

for ii = 1:numApertures
    %ii
    objLocal = big_obj( Ymin(ii):Ymax(ii), Xmin(ii):Xmax(
ii));
%    proj = probe_orig .* big_obj(oROI{ii,:}); % picks
out r-space region of model object
    exitWave = probeOrig .* objLocal;
    rdiffpats(:, :, ii) = exitWave; % full diff patt to

```

```

        compare super resolution with

diffpats (:, :, ii) = abs(fft2(exitWave)); % keep it
        already fftshift_michaled and squarerooted
diffpats_og (:, :, ii) = diffpats (:, :, ii); % record the
        origin pattern for comparison w noisy diff pats

if show_image
%       showim(abs(probe_orig.*big_obj(oROI{ii, :})));
        showim(abs(exitWave)); pause(0.5)
end

if diffpattnoise ~ = 0 % noisy
        diffpats (:, :, ii) = AddPNoise( abs(diffpats (:, :, ii
        )), diffpattnoise ) .* exp(1i*angle(diffpats
        (:, :, ii))); % noise free
end

if finite_CCD == 1 % super resolution
        diffpats (:, :, ii) = fftshift_michal(finiteCCD(
        fftshift_michal(diffpats (:, :, ii)), finiteratio*
        sizeCCD));
end

if beam_stop == 1 % missing center
        diffpats (:, :, ii) = fftshift_michal(beamstop(
        fftshift_michal(diffpats (:, :, ii)), stopsize));
        % beamstop
end

if ii == 1 && show_image
        figure(271)
        imagesc(fftshift_michal(diffpats (:, :, 1))), axis
        image
end
end
end

% HELPER FUNCTIONS

function positions = Grid_Scan(sizeObj, sizeCCD, side
)
    extent = (sizeObj - sizeCCD)/3;
    %extent = (sizeObj - sizeCCD)

```

```

xpos = linspace(-extent(1), extent(1), side);
ypos = linspace(-extent(2), extent(2), side);
[xpos_, ypos_] = meshgrid(xpos, ypos);

% add random offset
random_offset = 1;
if random_offset
    xpos_ = xpos_ + randn(size(xpos_)) * extent
        (1) / side / 3; % include variance in
        positions (normally distributed)
    ypos_ = ypos_ + randn(size(ypos_)) * extent
        (2) / side / 3;
end

xpos = round(xpos_(:) + sizeObj(2)/2+1);
ypos = round(ypos_(:) + sizeObj(1)/2+1);
positions = [xpos, ypos];
end

function g1 = Make_Circle_Mask(radius, imgSize)
    row=imgSize
    g1=zeros(row)
    w0=100;
    l=1;
    for ml=1:row
        for n1=1:row
            if (ml-row/2).^2+(n1-row/2).^2 < radius
                g1(ml,n1)=sqrt(((ml-row/2)^2+(n1-row/2)^2)^abs(l)*exp(-((
                    ml-row/2)^2+(n1-row/2)^2)/w0^2)*exp(1i*l*atan2((n1-row
                    /2), (ml-row/2)));
            end
        end
    end;
end
end

function [Xmin, Ymin, Xmax, Ymax] = Find_Scan_Area(
    positions, sizeCCD)
    ycen = round(positions(:,2));
    xcen = round(positions(:,1));
    Ymin = ycen - floor(sizeCCD(1)/2);
    Ymax = Ymin + sizeCCD(1) - 1; % coordinates
        covered in each scan position
    Xmin = xcen - floor(sizeCCD(2)/2);
    Xmax = Xmin + sizeCCD(2) - 1;
end

```

Bibliography

- [1] Chris Lee. Twisted light beats quantum light. [EB/OL]. <https://arstechnica.com/science/2013/12/twisted-light-beats-quantum-light/>.
- [2] Yali Wang, Tuo Li, Qiankun Gao, Sanguo Zhang, and Yishi Shi. Application of diffractive optical elements for controlling the light beam in ptychography. *Optical Engineering*, 52(9):091720, 2013.
- [3] TM Godden, R Suman, MJ Humphry, JM Rodenburg, and AM Maiden. Ptychographic microscope for three-dimensional imaging. *Optics express*, 22(10):12513–12523, 2014.
- [4] Yishi Shi, Tuo Li, Yali Wang, Qiankun Gao, Sanguo Zhang, and Haifei Li. Optical image encryption via ptychography. *Optics letters*, 38(9):1425–1427, 2013.
- [5] Guoan Zheng, Roarke Horstmeyer, and Changhui Yang. Wide-field, high-resolution fourier ptychographic microscopy. *Nature photonics*, 7(9):739–745, 2013.
- [6] R Bowman, V D’Ambrosio, E Rubino, O Jedrkiewicz, P Di Trapani, and Miles J Padgett. Optimisation of a low cost slm for diffraction efficiency and ghost order suppression. *The European Physical Journal Special Topics*, 199(1):149–158, 2011.
- [7] Weker. Ptychography. [EB/OL]. <https://sites.slac.stanford.edu/wekergroup/ptychography> Accessed October 4, 2020.
- [8] James P Kossin, Brian D McNoldy, and Wayne H Schubert. Vortical swirls in hurricane eye clouds. *Monthly Weather Review*, 130(12):3144–3149, 2002.
- [9] Shigeo Kida, S Goto, and T Makihara. Life, structure, and dynamical role of vortical motion in turbulence. *Tubes, Sheets and Singularities in Fluid Dynamics*, 2002.
- [10] Toshio Soda. Charge trapping by a vortex line in superfluid helium. *Progress of Theoretical Physics*, 36(3):435–444, 1966.

- [11] Les Allen, Marco W Beijersbergen, RJC Spreeuw, and JP Woerdman. Orbital angular momentum of light and the transformation of laguerre-gaussian laser modes. *Physical review A*, 45(11):8185, 1992.
- [12] Twisted Photons. Applications of light with orbital angular momentum, 2011.
- [13] Eleonora Nagali and Fabio Sciarrino. Manipulation of photonic orbital angular momentum for quantum information processing. *Advanced Photonic Sciences*, 4(1):75–103, 2012.
- [14] Miles Padgett and L Allen. Light with a twist in its tail. *Contemporary physics*, 41(5):275–285, 2000.
- [15] AM Stewart. Angular momentum of the electromagnetic field: the plane wave paradox resolved. *European journal of physics*, 26(4):635, 2005.
- [16] Enrique J Galvez. Gaussian beams in the optics course. *American journal of physics*, 74(4):355–361, 2006.
- [17] David S Simon. Bessel beams, self-healing, and diffraction-free propagation. *A Guided Tour of Light Beams: From lasers to optical knots*, pages 1–15, 2016.
- [18] David L Andrews and Mohamed Babiker. *The angular momentum of light*. Cambridge University Press, 2012.
- [19] Alison M Yao and Miles J Padgett. Orbital angular momentum: origins, behavior and applications. *Advances in Optics and Photonics*, 3(2):161–204, 2011.
- [20] Reiner Hegerl and W Hoppe. Dynamische theorie der kristallstruktur-analyse durch elektronenbeugung im inhomogenen primärstrahlwellenfeld. *Berichte der Bunsengesellschaft für physikalische Chemie*, 74(11):1148–1154, 1970.
- [21] W Hoppe and G Strube. Beugung in inhomogenen primärstrahlenwellenfeld. ii. lichtoptische analogieversuche zur phasemessung von gitterinterferenzen. *Acta Crystallographica Section A: Crystal Physics, Diffraction, Theoretical and General Crystallography*, 25(4):502–507, 1969.
- [22] JM Rodenburg and RHT Bates. The theory of super-resolution electron microscopy via wigner-distribution deconvolution. *Philosophical Transactions of the Royal Society of London. Series A: Physical and Engineering Sciences*, 339(1655):521–553, 1992.
- [23] P. Nellist, B. C. McCallum, and J. Rodenburg. Resolution beyond the 'information limit' in transmission electron microscopy. *Nature*, 374:630–632, 1995.

- [24] John M Rodenburg and Helen ML Faulkner. A phase retrieval algorithm for shifting illumination. *Applied physics letters*, 85(20):4795–4797, 2004.
- [25] JM Rodenburg, AC Hurst, and AG Cullis. Transmission microscopy without lenses for objects of unlimited size. *Ultramicroscopy*, 107(2-3):227–231, 2007.
- [26] JM Rodenburg, AC Hurst, AG Cullis, BR Dobson, F Pfeiffer, O Bunk, C David, K Jefimovs, and I Johnson. Hard-x-ray lensless imaging of extended objects. *Physical review letters*, 98(3):034801, 2007.
- [27] Pierre Thibault, Martin Dierolf, Andreas Menzel, Oliver Bunk, Christian David, and Franz Pfeiffer. High-resolution scanning x-ray diffraction microscopy. *Science*, 321(5887):379–382, 2008.
- [28] Martin Dierolf, Andreas Menzel, Pierre Thibault, Philipp Schneider, Cameron M Kewish, Roger Wepf, Oliver Bunk, and Franz Pfeiffer. Ptychographic x-ray computed tomography at the nanoscale. *Nature*, 467(7314):436–439, 2010.
- [29] MJ Humphry, B Kraus, AC Hurst, AM Maiden, and JM Rodenburg. Ptychographic electron microscopy using high-angle dark-field scattering for sub-nanometre resolution imaging. *Nature communications*, 3(1):1–7, 2012.
- [30] AM Maiden, JM Rodenburg, and MJ Humphry. A new method of high resolution, quantitative phase scanning microscopy. In *Scanning Microscopy 2010*, volume 7729, page 77291I. International Society for Optics and Photonics, 2010.
- [31] Manuel Guizar-Sicairos, Samuel T Thurman, and James R Fienup. Efficient subpixel image registration algorithms. *Optics letters*, 33(2):156–158, 2008.
- [32] John M Rodenburg. Ptychography and related diffractive imaging methods. *Advances in imaging and electron physics*, 150:87–184, 2008.
- [33] Yali Wang, Tuo Li, Qiankun Gao, Sanguo Zhang, and Yishi Shi. Application of diffractive optical elements for controlling the light beam in ptychography. *Optical Engineering*, 52(9):1442–1450, 2013.
- [34] Pierre Thibault, Martin Dierolf, Oliver Bunk, Andreas Menzel, and Franz Pfeiffer. Probe retrieval in ptychographic coherent diffractive imaging. *Ultramicroscopy*, 109(4):338–343, 2009.
- [35] Lord Rayleigh. Xxxi. investigations in optics, with special reference to the spectroscope. *The London, Edinburgh, and Dublin Philosophical Magazine and Journal of Science*, 8(49):261–274, 1879.
- [36] Max Born and Emil Wolf. Principles of optics, 7th (expanded) edition. *United Kingdom: Press Syndicate of the University of Cambridge*, 461, 1999.

- [37] O Scherzer. Some defects of electron lenses. *Z. Phys*, 101(9-10):593–603, 1936.
- [38] Ralph W Gerchberg. A practical algorithm for the determination of phase from image and diffraction plane pictures. *Optik*, 35:237–246, 1972.
- [39] David Sayre. Some implications of a theorem due to shannon. *Acta Crystallographica*, 5(6):843–843, 1952.
- [40] Dennis Gabor. A new microscopic principle, 1948.
- [41] Etienne Cuche, Frédéric Bevilacqua, and Christian Depeursinge. Digital holography for quantitative phase-contrast imaging. *Optics letters*, 24(5):291–293, 1999.
- [42] Etienne Cuche, Pierre Marquet, and Christian Depeursinge. Simultaneous amplitude-contrast and quantitative phase-contrast microscopy by numerical reconstruction of fresnel off-axis holograms. *Applied optics*, 38(34):6994–7001, 1999.
- [43] Giancarlo Pedrini, Hans J Tiziani, and Mikhail E Gusev. Pulsed digital holographic interferometry with 694-and 347-nm wavelengths. *Applied optics*, 39(2):246–249, 2000.
- [44] Songcan Lai and Mark A Neifeld. Digital wavefront reconstruction and its application to image encryption. *Optics communications*, 178(4-6):283–289, 2000.
- [45] Bahram Javidi and Enrique Tajahuerce. Three-dimensional object recognition by use of digital holography. *Optics Letters*, 25(9):610–612, 2000.
- [46] Myung-Keun Kim. Tomographic three-dimensional imaging of a biological specimen using wavelength-scanning digital interference holography. *Optics Express*, 7(9):305–310, 2000.
- [47] Heather I Campbell, Sijiong Zhang, Alan H Greenaway, and Sergio Restaino. Generalized phase diversity for wave-front sensing. *Optics letters*, 29(23):2707–2709, 2004.
- [48] Jianwei Miao, David Sayre, and HN Chapman. Phase retrieval from the magnitude of the fourier transforms of nonperiodic objects. *JOSA A*, 15(6):1662–1669, 1998.
- [49] W Hoppe. Diffraction in inhomogeneous primary wave fields. 3. amplitude and phase determination for nonperiodic objects. *Acta Crystallographica Section a-Crystal Physics Diffraction Theoretical and General Crystallography*, page 508, 1969.

- [50] W Hoppe. Diffraction in inhomogeneous primary wave fields. 1. principle of phase determination from electron diffraction interference. *Acta Crystallographica Section a-Crystal Physics Diffraction Theoretical and General Crystallography*, page 495, 1969.
- [51] Helen Mary Louise Faulkner and JM Rodenburg. Movable aperture lensless transmission microscopy: a novel phase retrieval algorithm. *Physical review letters*, 93(2):023903, 2004.
- [52] M Born and E Wolf. Book review: Principles of optics.-7th expanded ed./cambridge u press, 1999. *The Observatory*, 120:149, 2000.
- [53] VS Ignatowsky. Diffraction by a lens of arbitrary aperture. *Trans. Opt. Inst*, 1(4):1–36, 1919.
- [54] W Braunbek and G Laukien. Features of refraction by a semi-plane. *Optik*, 9:174–179, 1952.
- [55] Bernard Richards and Emil Wolf. Electromagnetic diffraction in optical systems, ii. structure of the image field in an aplanatic system. *Proceedings of the Royal Society of London. Series A. Mathematical and Physical Sciences*, 253(1274):358–379, 1959.
- [56] A Boivin, J Dow, and E Wolf. Energy flow in the neighborhood of the focus of a coherent beam. *JOSA*, 57(10):1171–1175, 1967.
- [57] John Frederick Nye and Michael Victor Berry. Dislocations in wave trains. *Proceedings of the Royal Society of London. A. Mathematical and Physical Sciences*, 336(1605):165–190, 1974.
- [58] MS Soskin and MV Vasnetsov. Singular optics. *Progress in optics*, 42(4):219–276, 2001.
- [59] NB Baranova, B Ia Zeldovich, AV Mamaev, NF Pilipetskii, and VV Shkunov. An investigation of the dislocation density of a wave front in light fields having a speckle structure. *ZhETF*, 83:1702–1710, 1982.
- [60] P Couillet, L Gil, and F Rocca. Optical vortices. *Optics Communications*, 73(5):403–408, 1989.
- [61] GA Swartzlander Jr and CT Law. Optical vortex solitons observed in kerr nonlinear media. *Physical Review Letters*, 69(17):2503, 1992.
- [62] H He, MEJ Friese, NR Heckenberg, and H Rubinsztein-Dunlop. Direct observation of transfer of angular momentum to absorptive particles from a laser beam with a phase singularity. *Physical review letters*, 75(5):826, 1995.
- [63] NB Simpson, K Dholakia, L Allen, and MJ Padgett. Mechanical equivalence of spin and orbital angular momentum of light: an optical spanner. *Optics letters*, 22(1):52–54, 1997.

- [64] Yi Zhou, Shaotong Feng, Shouping Nie, Jun Ma, and Caojin Yuan. Image edge enhancement using airy spiral phase filter. *Optics Express*, 24(22):25258–25268, 2016.
- [65] Manuel Erhard, Robert Fickler, Mario Krenn, and Anton Zeilinger. Twisted photons: new quantum perspectives in high dimensions. *Light: Science & Applications*, 7(3):17146–17146, 2018.
- [66] Li Lu, Wen Sheng, Feng Jiang, and Zengjun Bi. Propagation characteristics of orbital angular momentum for remote imaging. In *Optoelectronic Imaging and Multimedia Technology IV*, volume 10020, page 100200T. International Society for Optics and Photonics, 2016.
- [67] Henry N Chapman. A new phase for x-ray imaging. *Nature*, 467(7314):409–410, 2010.
- [68] Tim Salditt. X-ray imaging at the nanoscale: ptychography, holography and tomography. 2016.
- [69] M Odstrčil, P Baksh, and WS Brocklesby. Coherent diffraction imaging using laboratory light sources. 2014.
- [70] Adam Kozma and David Lee Kelly. Spatial filtering for detection of signals submerged in noise. *Applied Optics*, 4(4):387–392, 1965.
- [71] Adolph W Lohmann and DP Paris. Binary fraunhofer holograms, generated by computer. *Applied optics*, 6(10):1739–1748, 1967.
- [72] JJ Burch. A computer algorithm for the synthesis of spatial frequency filters. *Proceedings of the IEEE*, 55(4):599–601, 1967.
- [73] LB Lesem, PM Hirsch, and JA Jordan. Generation of discrete-point holograms. In *Journal Of The Optical Society Of America*, volume 58, page 729. Amer Inst Physics Circulation Fulfillment Div, 500 Sunnyside Blvd, Woodbury, 1968.
- [74] Wai-Hon Lee. Binary synthetic holograms. *Applied optics*, 13(7):1677–1682, 1974.
- [75] CB Burckhardt. A simplification of lee’s method of generating holograms by computer. *Applied optics*, 9(8):1949–1949, 1970.
- [76] MJ Snadden, AS Bell, RBM Clarke, E Riis, and DH McIntyre. Doughnut mode magneto-optical trap. *JOSA B*, 14(3):544–552, 1997.
- [77] IV Basistiy, V Yu Bazhenov, MS Soskin, and M Vu Vasnetsov. Optics of light beams with screw dislocations. *Optics communications*, 103(5-6):422–428, 1993.
- [78] V Yu Bazhenov, MV Vasnetsov, and MS Soskin. Laser beams with screw dislocations in their wavefronts. *Jetp Lett*, 52(8):429–431, 1990.

- [79] NR Heckenberg, R McDuff, CP Smith, and AG White. Generation of optical phase singularities by computer-generated holograms. *Optics letters*, 17(3):221–223, 1992.
- [80] Carl Paterson and Robin Smith. Higher-order bessel waves produced by axicon-type computer-generated holograms. *Optics Communications*, 124(1-2):121–130, 1996.
- [81] Jennifer E Curtis and David G Grier. Structure of optical vortices. *Physical review letters*, 90(13):133901, 2003.
- [82] Jennifer E Curtis and David G Grier. Modulated optical vortices. *Optics letters*, 28(11):872–874, 2003.
- [83] Chao Yang, Jianliang Qian, Andre Schirotzek, FRNC Maia, and Stefano Marchesini. Iterative algorithms for ptychographic phase retrieval. *arXiv preprint arXiv:1105.5628*, 2011.
- [84] Jianliang Qian, Chao Yang, A Schirotzek, F Maia, and S Marchesini. Efficient algorithms for ptychographic phase retrieval. *Inverse Problems and Applications, Contemp. Math*, 615:261–280, 2014.
- [85] Oliver Bunk, Martin Dierolf, Søren Kynde, Ian Johnson, Othmar Marti, and Franz Pfeiffer. Influence of the overlap parameter on the convergence of the ptychographical iterative engine. *Ultramicroscopy*, 108(5):481–487, 2008.
- [86] Andrew M Maiden and John M Rodenburg. An improved ptychographical phase retrieval algorithm for diffractive imaging. *Ultramicroscopy*, 109(10):1256–1262, 2009.
- [87] F Hüe, JM Rodenburg, AM Maiden, and PA Midgley. Extended ptychography in the transmission electron microscope: Possibilities and limitations. *Ultramicroscopy*, 111(8):1117–1123, 2011.
- [88] Holoeye. Pluto-2.1-vis-016 manual. web. <https://holoeye.com/slm-pluto-phase-only/> Accessed December 4, 2020.
- [89] Joseph W Goodman. *Introduction to Fourier optics*. Roberts and Company Publishers, 2005.
- [90] mathwork. Psnr. [EB/OL]. [https://www.mathworks.com/help/vision/ref/psnr.html#:~:text=The%20mean%2Dsquare%20error%20\(MSE,MSE%2C%20the%20lower%20the%20error](https://www.mathworks.com/help/vision/ref/psnr.html#:~:text=The%20mean%2Dsquare%20error%20(MSE,MSE%2C%20the%20lower%20the%20error). Accessed October 4, 2020.
- [91] Zhou Wang, Alan C Bovik, and Eero P Simoncelli. Structural approaches to image quality assessment. *Handbook of image and video processing*, 7(18), 2005.

- [92] Fang Gui-Juan and Pu Ji-Xiong. Propagation properties of stochastic electromagnetic double-vortex beams in a turbulent atmosphere. *Chinese Physics B*, 21(8):084203, 2012.
- [93] Eugene Hecht. *Optics*. Addison-Wesley, 4 edition, 2002.
- [94] Eugene Hecht. *Optics*. Addison-Wesley, 4 edition, 2002.